IDEA League

Master of Science in Applied Geophysics

Research Thesis

Full waveform inversion of the African crust and mantle: strategies for accelerating model convergence

Dirk-Philip van Herwaarden

August 26, 2016

Full waveform inversion of the African crust and mantle: strategies for accelerating model convergence

Master of Science Thesis

for the degree of Master of Science in Applied Geophysics at
Delft University of Technology
ETH Zürich
RWTH Aachen University
by

Dirk-Philip van Herwaarden

August 26, 2016

Department of Geoscience & Engineering · Delft University of Technology
Department of Earth Sciences · ETH Zürich
Faculty of Georesources and Material Engineering · RWTH Aachen University

Eidgenössische Technische Hochschule Zürich
Swiss Federal Institute of Technology Zurich

Printed in The Netherlands, Switzerland, Germany

IDEA LEAGUE
JOINT MASTER'S IN APPLIED GEOPHYSICS

Delft University of Technology, The Netherlands
ETH Zürich, Switzerland
RWTH Aachen, Germany

Dated: *August 26, 2016*

Supervisor(s):

Andreas Fichtner

Michael Afanasiev

Committee Members:

Andreas Fichtner

Michael Afanasiev

Evert Slob

Abstract

The continent of Africa is one of the most geophysically interesting regions on the planet. More specifically, Africa contains the Afar Depression, which is the only place on Earth where incipient sea-floor spreading is sub-aerially exposed, along with other anomalous features such as the unexplained topography in the south. Despite its geophysical significance, relatively few tomographic images exist of Africa. This stems mainly from the sparse distribution of seismic monitoring stations on the continent, which itself is a result of the political instability and general geographical remoteness. As a result, the debate on the geophysical origins of Africa's anomalies is rich and ongoing. In this project a tomographic image is produced using the technique of elastic Full Waveform Inversion (FWI). To our knowledge this is the first attempt at performing a continental-scale FWI of the region. Data recorded from 100 earthquakes has been used as input for the inversion. The adjoint method was used to iteratively update the initial model, which was extracted from the Collaborative Seismic Earth Model. Forward and adjoint modelling were performed in the regional version of SPECFEM3D_GLOBE, a global wave propagation solver based on the spectral element method. Over the course of ten iterations, the time-frequency phase misfit decreased satisfactorily, and additional details were added to the starting model. The final model was validated by evaluating the change in misfit for ten earthquakes not previously used in the inversion. All of these events showed a decrease in misfit.

Acknowledgements

Firstly, I want to thank my two excellent supervisors: Andreas Fichtner and Michael Afanasiev. Andreas for arousing my interest towards inversion methods in last year's inversion courses and for making it possible to write this thesis here at ETH. I was amazed of how quick he was to answer all of my questions, even while he was obviously involved in so many other things. This really inspired me. I am very grateful to have had Mike as a supervisor. I really enjoyed working with him. He was always there to answer my often trivial questions and help me throughout the project. Without his support, I wouldn't have come near as far and learned near as much. I couldn't have wished for better supervisors. I am also thankful for having been part of the Computational Seismology group. I really enjoyed the Tuesday cakes and bi-weekly seminars. They brought a healthy dose of variation to the week. It was interesting and motivating to learn about the projects everyone was working on.

Secondly, I want to thank everyone else who has been directly or indirectly involved in the project. To start with the Swiss National Supercomputing Centre (CSCS), for allowing me to use their supercomputer Piz Daint. Also their help desk was very helpful, whenever I ran into problems. I also want to thank Jeroen Tromp and Dimitri Komatitsch and their groups for the work they did in developing the global wave propagation solver SPECFEM3D_GLOBE, that has been used for this project. Daniel Peter for helping me out so kindly, when I faced bugs in the adjoint simulations of the regional version. I also want to thank everyone who contributed to the acquisition of data in Africa, especially Andy Nyblade who had a big impact on the development of the AfricaArray and IRIS, which made the data accessible. Without the seismic data, this work would have been impossible. Furthermore I want to thank Lion Krischer and others who were involved in developing tools such as Obspy and LASIF, which made it much easier to perform this work. Patrick Paitz for providing me with ambient seismic noise cross-correlations and all the others who contributed.

Thirdly, I want to thank everyone else that helped to make this possible. My friends and family, who have always been there to support me, irrespective of what I do. My fellow students in F21, for the coffee breaks and for letting me know I was not the only one struggling at times. And finally Christine, for coming with me to Zurich and making life so much more enjoyable.

ETH Zürich
August 26, 2016

Dirk-Philip van Herwaarden

Table of Contents

Abstract v

Acknowledgements vii

Acronyms xi

1 Introduction 1

1-0-1 Geological background . . . 2

2 Data selection and processing 5

2-1 Introduction . . . 5

2-2 Selecting a time window for the earthquake events . . . 5

2-3 Selecting Earthquake events . . . 6

2-4 Downloading Seismic Data . . . 6

2-5 Preprocessing the Seismic Data . . . 7

3 Full Waveform Inversion: Theory and Application 11

3-1 Introduction . . . 11

3-1-1 Inversion Basics . . . 12

3-2 The Forward Problem . . . 13

3-2-1 Governing Equations . . . 13

3-2-2 Solver: SPECFEM3D_GLOBE . . . 15

3-2-3 Initial model . . . 16

3-3 The Adjoint Method . . . 17

3-3-1 Misfits . . . 21

3-3-2 Window selection . . . 21

3-3-3 Creating Adjoint sources . . . 22

3-3-4 Kernel Simulation . . . 23

3-4 Improving convergence: station weighting 23
3-5 Model update 24
3-5-1 Step length search 24
3-6 Results 25
3-6-1 Validation 36
3-7 Discussion 38
3-8 Conclusion 41

Bibliography **43**

A Used Data **49**
A-1 Events 49
A-2 Stations 51

B Solver Parameter file **61**

Acronyms

DUT Delft University of Technology

ETH Swiss Federal Institute of Technology

RWTH Aachen University

FWI Full Waveform Inversion

CSEM Collaborative Seismic Earth Model

LASIF LArge-scale Seismic Inversion Framework

EARS East African Rift System

AD Afar Depression

GLL Gauss-Lobatto-Legendre

IRIS Incorporated Research Institutions for Seismology

Chapter 1

Introduction

The seismic structure of Africa remains poorly understood, mainly because of the sparse distributions of seismic stations and the large aseismic areas. This makes it challenging to obtain high quality images. Some regionally focused studies have been performed in Africa, but for large parts little is known about the seismic structure of the lithosphere. What is known about the seismic structures stems mostly from large scale global and regional studies. In an early study Dziewonski (1984) revealed thick seismically fast keels beneath Africa's cratonic regions. More recently, studies by Ritsema et al. (1999); Ritsema and van Heijst (2000); Pasyanos and Nyblade (2007) provided images of the cratonic keels in more detail.

In this thesis an attempt is made to improve the current state of models of the seismic structure beneath Africa. As far as we are aware, it will be the first attempt to do that using the method of *Full Waveform Inversion* (FWI). The inversion parameters are v_{SV}, v_{SH}, v_{PV} and the anisotropy parameter η as defined by Dziewonski and Anderson (1981). As a starting model, we use the Collaborative Seismic Earth Model (CSEM) Afanasiev et al. (2016). To model the elastic waves, the regional version of SPECFEM3D_GLOBE Spe (2016a) is used. Seismic data and synthetics are bandpass filtered such that the dominant wave periods fall between 40 s and 100 s. This relatively long wavelength is used for two reasons. Firstly, using long wavelengths helps to ensure the inverse problem converges to the global minimum. The phase shift between simulated and recorded data should not be more than half a period from the recorded data. With longer wavelengths this happens less quickly. Another reason to use the relative long wavelength is the decreased computational cost of modelling an earthquake event. With a certain amount of node hours available a trade off has to be made between the amount of earthquake events that can be modelled and the element size of the used mesh. A finer mesh means modelling smaller wavelengths, thus possible higher resolution, but comes at the cost of less sensitivity coverage and a higher computational cost for each iteration.

The reason to focus on Africa in particular, is that still relatively little is known in terms of the subsurface structures compared to other continents. Improving the model of Africa would not only be useful for filling a gap of resolution in the CSEM, but also help geologists and geodynamicists to gain a better understanding of the continent. As Fishwick and Bastow (2011) mentions: seismic data can help constrain a number of factors that are fundamental

to some of Africa's more puzzling geophysical features, e.g. the anomalously high topography present in the southern regions. The velocities in the mantle found through seismic tomography can be interpreted in terms of variations in temperature or buoyancy. Estimating crustal thickness helps to constrain which portion of the topography is attributed to *isostasy*, the elevation of the crust that is expected due to the density and weight of the crust. Seismic anisotropy helps to place constraints on the direction of mantle flow. Given constraints on the Lithosphere-Asthenosphere Boundary (LAB) geodynamicists can model more subtle effects on topography from mantle convection.

The structure of the thesis is as follows: First the introduction will continue with a short geological background on the origins of Africa and the structures that are potentially visible. In Chapter 2, the selection and processing of the data that is used for the inversion is described. This includes finding a good time period in which to select earthquakes, downloading the seismic data and preprocessing it. This chapter is mostly targeted towards those who are interested in the ray coverage achieved, and which tools a dataset can be acquired. In Chapter 3, the steps involved in a Full Waveform Inversion are explained and results are shown, along with the individual steps. Starting from a quick introduction to what inversion means in general, we then discuss the forward and adjoint problems which rely on solving the elastic wave equation within an Earth model. Following the forward problem, the adjoint method is discussed, which is used to find the gradient to the misfit functional. Volumetric densities of the gradient to the misfit functional, also called kernels are generated from the kernel simulations. Methods are discussed to improve the meaningfulness and quality of the kernels. The kernels are smoothed and adjoint sources are weighted based on their distances to other adjoint sources to obtain a more balanced kernel. With the balanced kernels in place, the model can be updated using gradient methods. The first update is of the steepest descent type, with the step length found using the line-search method. This process from forward modelling to finding the gradient and step length is repeated for several iterations to find a model with a misfit closer to the global minimum. The results from the procedure are shown and described. A test is performed with an independent set of earthquakes to validate the model. The thesis concludes with a discussion and conclusion.

1-0-1 Geological background

In this section a brief review of the history and major tectonic features of Africa is given. Despite the fact that relatively little is known about the seismic structures, it is a geophysically very interesting region. For example the Afar Depression, which is the only place on Earth where incipient sea-floor spreading is sub-aerially exposed Makris and Ginzburg (1987).

The Pan-African orogeny (500-600 Ma) brought together the cratons that still form the basis of the African continent today. The West African Craton, Congo Craton, Kalahari Craton and Tanzania craton came together to form Gondwana and thereafter Pangaea. Africa was at the heart of the supercontinent Pangaea before it was split up through the opening of the Central Atlantic Torsvik et al. (2008), South Atlantic Torsvik et al. (2009) and Indian Cande et al. (2010) Oceans. These events together with the subductions that occurred in the north roughly shaped the continent. However, many questions remain. E.g. for a region that is mostly surrounded by extensional plate boundaries there is significant topography that cannot fully be explained with plate tectonic theory.

Doucouré and de Wit (2003) describe the dominant first order feature as a near bimodal topography which has elevated regions (500 to 3000 m, average = 1015 m) in Eastern and Southern Africa and a more subdued terrain of Central-West and West Africa (300 -1500 m, average = 450m). They infer this near-bimodality of Africa's topography is an ancient feature inherited from Upper Paleozoic times or earlier. Superimposed on the long-wavelength features described by Doucouré and de Wit (2003) are a number of basins and swells as described in Duff and Duff (1993). Figure 1-1 shows the major tectonic features superimposed on the regional topography. When the results are shown in Chapter 3 it can be helpful to keep these tectonic features in mind, both for description and interpretation purposes.

Suggestions have been made that the topography in North-Western Africa could have a dynamic cause such as mantle upwellings, e.g. Teixell et al. (2005). In other regions other factors such as the emplacement of volcanic rock during hotspot tectonism, crustal thinning and rift flank flexure, during extensional tectonics such as the East African Rift could have an effect Fishwick and Bastow (2011). Another significant feature that has been suggested to exist is a whole mantle-mantle superplume structure beneath Eastern Africa Mulibo and Nyblade (2013). Readers who are interested in getting a more comprehensive overview of the African Geology and tectonics are referred to Burke (1996) and Cahen et al. (1984).

Readers who wish to compare the results of this study to other seismic studies are referred to Fishwick and Bastow (2011), which gives an excellent overview of many existing studies. They also highlight key seismic observations and suggest methodologies that will help to improve links between seismological and topographic variations and thus improve our certainty of understanding. Apart from other applications of an improved tomographic image, their request for continent-wide higher resolution measurements is an important part of the motivation for this research.

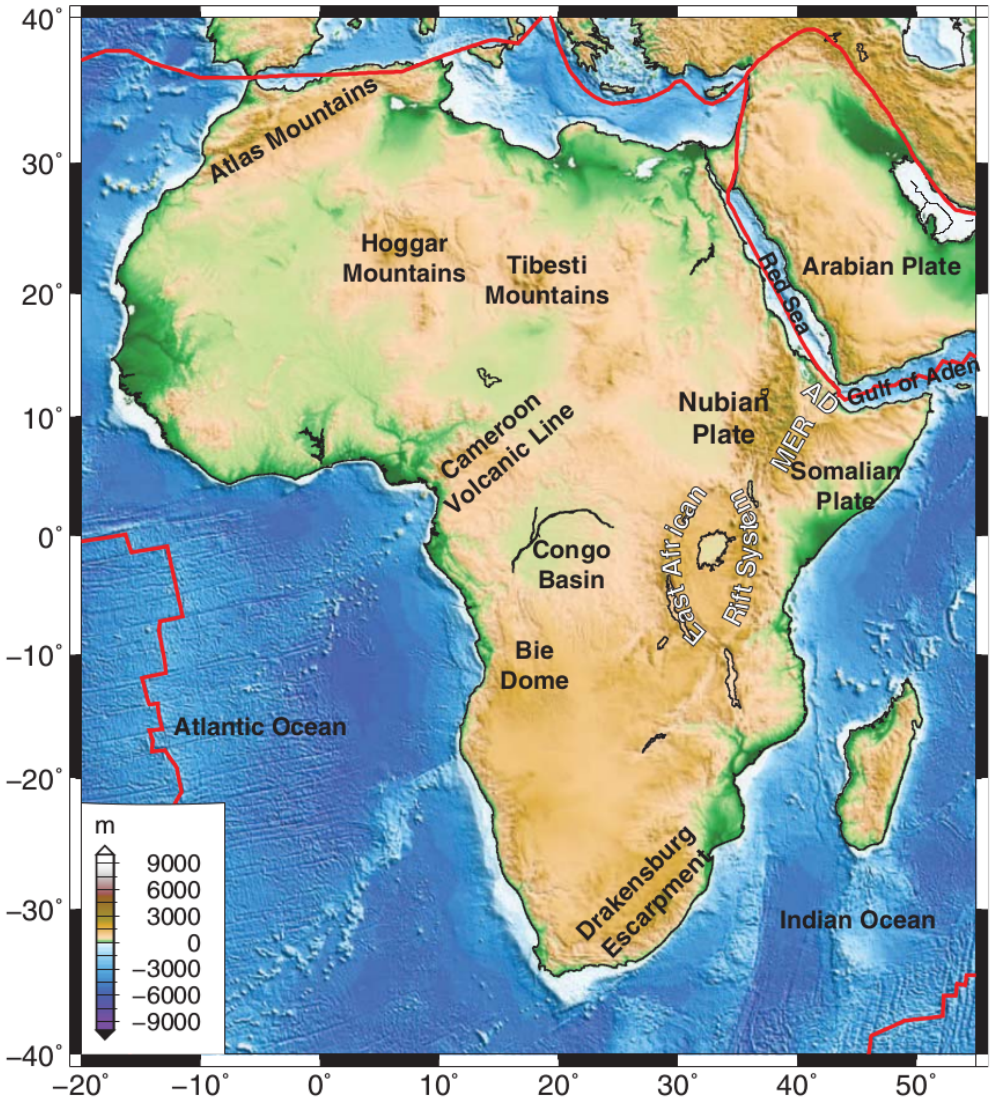

Figure 1-1: Map of Africa showing major tectonic features superimposed on the regional topography, such as the anomalously high topography in the south and the AD. (MER: Main Ethiopian Rift; AD, Afar Depression. Source: Fishwick and Bastow (2011)

Chapter 2

Data selection and processing

2-1 Introduction

In this chapter all the steps taken for this project regarding the data selection and processing will be discussed. The goal of this chapter is to inform the reader which data has been used and how it has been processed for this study, and also act as a guide to inform a possible future student on how this can be done and which tools are useful. Since the results obtained by full waveform inversion strongly depend on the amount and quality of the data used, decisions made regarding data selection and processing are very important. This study uses earthquake data, but since each event is modelled separately and there is a limit in computational power, it is useful to spend some effort to try to select only the best data available. This means obtaining a good spatial distribution for the earthquakes and that during each of these events a high amount of recording stations are online with a proper distribution. In the case of Africa, where there is comparatively little data because of the political instability and general remoteness, this becomes even more important. First the optimal time period is selected to get the best data. Based on this time period the events with the best spatial distribution will be selected. Finally the data is downloaded and preprocessed such that it is ready for the FWI described in Chapter 3.

2-2 Selecting a time window for the earthquake events

The first important step for this study was to find a time range, for which earthquake events will be selected. Arrays in Africa are not as stably operated as in the US or Europe. Arrays are deployed, but when funding stops or the political situation changes, which tends to happen quite often in the region, stations are removed. The amount of stations and their distribution has changed wildly over time. Since there are limitations on computational resources, it is beneficial to only use earthquake events that actually have been recorded by a stations with a spread in their geographical distribution. To tackle this problem the starting point was to generate a list of all the stations that have been deployed with their respective begin and

end times. This information, as well as the seismic data, is available from IRIS IRI (2016). Using this information a time-lapse was made showing all the stations over time. Figure 2-1 illustrates the importance of looking at station coverage over time before selecting earthquake events. The best coverage in terms of amount of stations and regional distribution was found in the period of 2010 to 2015. This knowledge was then used to select earthquake events.

(a) 1997 **(b)** 2004 **(c)** 2013

Figure 2-1: Snapshots of the used time-lapse to select a good time range, figures are showing 1997, 2004 and 2013 respectively. Blue dots represent station locations.

2-3 Selecting Earthquake events

Based on the previously found optimal time window, earthquakes were selected between the years of 2010 and 2015. The goal is to get an optimal distribution of earthquakes over the region of interest. To achieve this, LASIF (Large–Scale Seismic Inversion Framework) Krischer et al. (2015a) was used. LASIF is a data–driven end–to–end workflow tool to perform adjoint full seismic waveform inversions. Figure 2-2 shows the selected earthquake events and the region of interest. As can be seen, the events form a large circle around Africa with most events located at the boundaries of the African plate. Fortunately for the African people, but unfortunate for this study there are not many earthquakes occurring in the middle of Africa of an appropriate magnitude. The earthquakes will be modelled as point sources, an approximation which becomes less accurate for larger earthquake magnitudes. Therefore a maximum magnitude of 6.7 was used. A minimum magnitude of 5.5 was used, as smaller magnitude earthquakes would result in a lower signal-to-noise ratios because of the associated weaker signal.

2-4 Downloading Seismic Data

Once earthquakes were selected, the next step is to gather the raw data. Since going through each event manually and downloading the right stations is just one of the possible tedious tasks, a work-flow management tool was developed for this project called OvalOffice. This

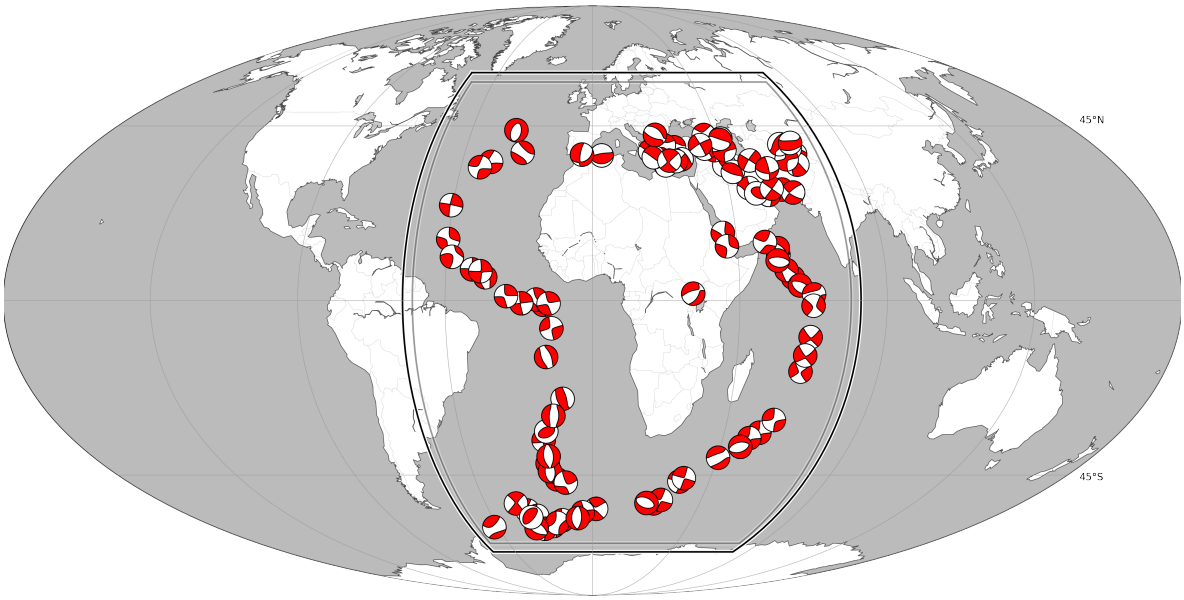

Figure 2-2: Selected earthquake events using beach ball representation.

tool which can be obtained from GitHub Ova (2016) automates many of the otherwise time-consuming processes. OvalOffice calls functions from ObsPy Beyreuther et al. (2010); Krischer et al. (2015b) to connect to IRIS and download the raw data, for a specified length of time for each earthquake event. We attempted to download 45 minutes worth of data. The stations for which data was acquired are visualized in Figure 2-3.

The resulting ray density is shown in Figure 2-4. The image suggests that we have good ray coverage, but unfortunately this is an artefact of scale. The modelled region remains sparsely covered and therefore extra care needs to be taken during the inversion.

2-5 Preprocessing the Seismic Data

With all the station data present, the final step required before the data can be used for the full waveform inversion, is to preprocess each seismic trace for each station. An example of a raw recording of a seismogram is shown in Figure 2-5. Basic checks are performed on the downloaded data before it will be used for the inversion, e.g. the recording length is required to be at least as long as the simulation time specified in the solver. In chapter 3 the choice of solver will be discussed in more detail. When checks regarding data availability are passed, the seismogram is trimmed to match the simulation time in the parameter file of the solver SPECFEM3D_GLOBE, see Appendix B. The trimming is performed to reduce the data usage and computational cost of all future preprocessing steps. Following these basic steps the data is decimated by a factor n to bring the sampling rate down to the sampling rate of the synthetics, which is sampled every 0.15 s. The decimation is performed to reduce the further cost of processing. Before down sampling, a low-pass filter is applied to remove the high-frequency components that could cause aliasing. Linear trend and mean are removed from each trace, which removes very low frequency noise.

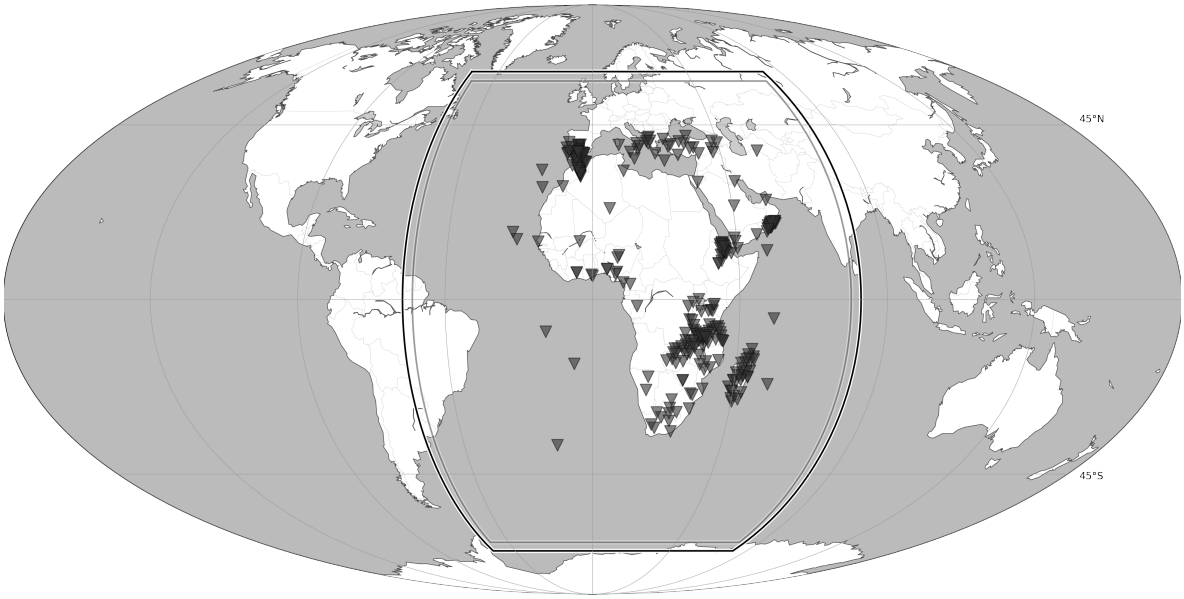

Figure 2-3: All the stations from which raw data was acquired are represented by grey triangles. The thicker lines surrounding Africa show the modelled domain.

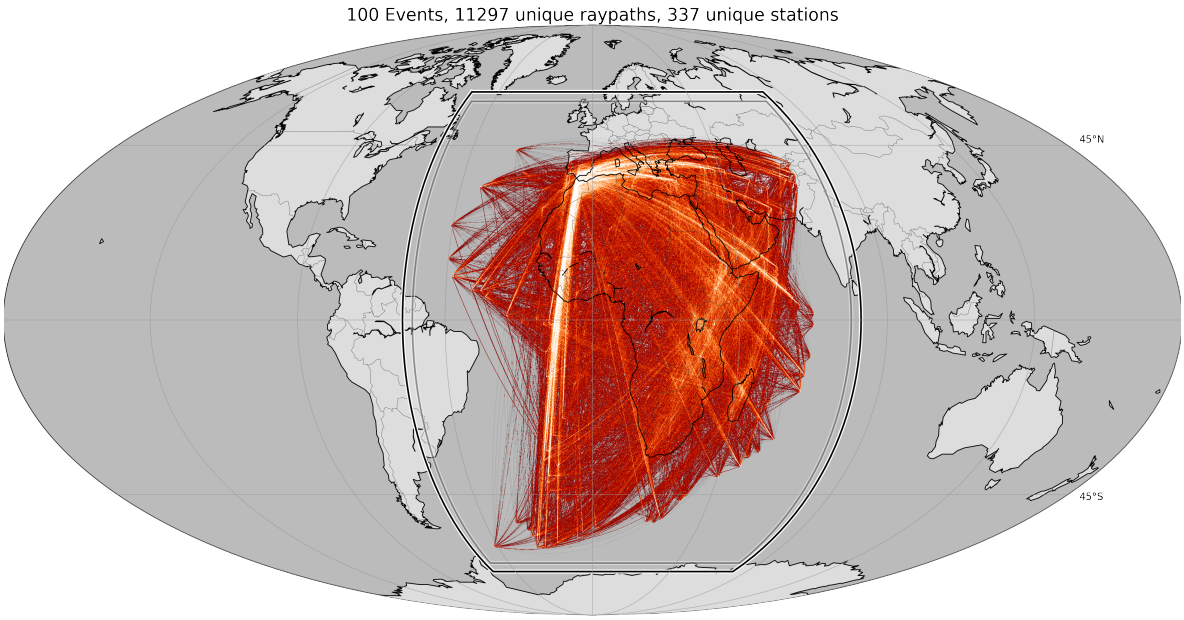

Figure 2-4: An image of the ray coverage, bright colors indicate a higher ray density.

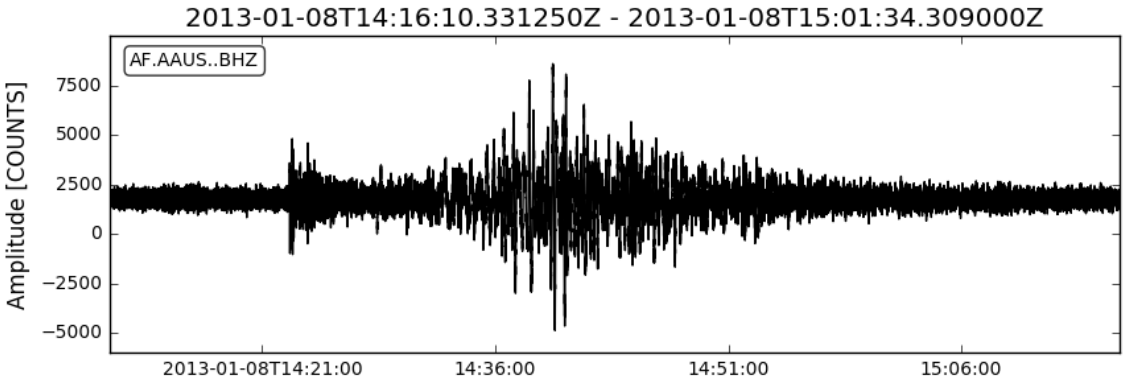

Figure 2-5: Raw recordings of the Z-component at station AF.AAUS, during the Aegean Sea earthquake (Mag 5.8 2013-1-8-14).

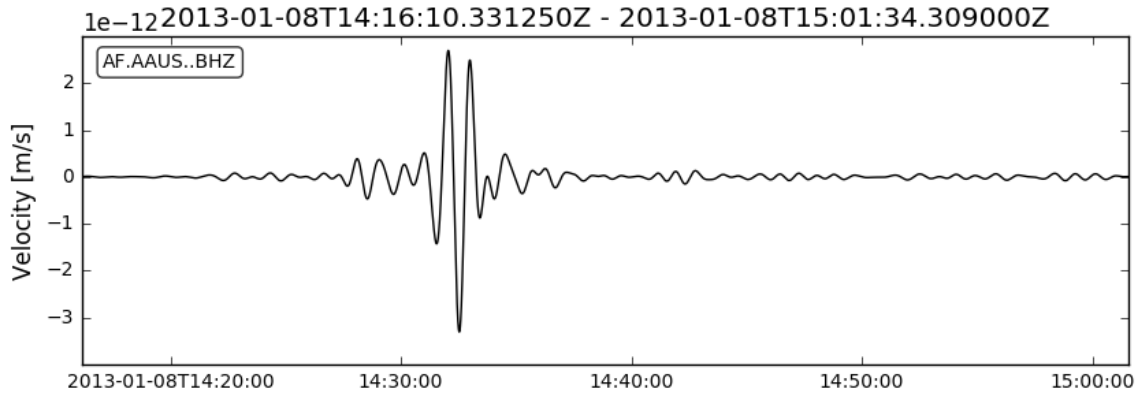

Figure 2-6: Preprocessed recordings from the same station as shown in Figure 2-5.

To reduce spectral leakage, both edges of the seismogram are tapered with a cosine taper that is 5% of the trace length. The next step in preprocessing is the instrument response removal, which attempts to flatten the response across frequencies and converts measurements to units of m/s. After which the data is bandpass filtered to get the data in the frequency band of interest. For this study the 40 seconds to 100 seconds wave periods were kept. These fairly long periods were chosen to reduce computational expenses and loosen the requirements of an accurate starting model. The final step is to interpolate, using the Lanczos method to match the sampling rate of the preprocessed data, with that of synthetics generated by the solver. Extensive use was made of both Obspy Krischer et al. (2015b) and Scipy Jones et al. (2001). For interested readers, the exact preprocessing script can be found in the OvalOffice repository on GitHub Ova (2016).

Chapter 3

Full Waveform Inversion: Theory and Application

3-1 Introduction

In this chapter a brief introduction to the method of Full Waveform Inversion (FWI) is given, along with a step-by-step plan to achieve the final results presented in this thesis. The necessary steps that are required in the FWI process will be explained as well as how these steps were performed in this study.

For a scientist one of the most important characteristics of seismic waves is that they contain information. A recorded seismogram contains information of the seismic source and the medium through which the waves have travelled. The goal for a scientist is to extract the desired and available information in an efficient and meaningful manner to get a better understanding of the world surrounding us. Since probably the first active source seismic experiments, performed by R. Mallet (1810-1881) and his son J.W. Mallet (1832-1912) between 1852 and 1858 Mallet and Mallet (1858), where they measured wave propagation speeds using gun power explosions, seismology has greatly evolved. Major discoveries regarding the internal structure of the planet arose in the first half of the 20th century using travel time information. R.D. Oldham (1958-1936) discovered the existence of the Earth's outer core Oldham (1906), the depth of which was first correctly estimated by B. Gutenberg (1889-1960) Gutenberg (1913). In 1936 I. Lehmann (1988-1993) discovered the existence of the solid inner core inside the molten outer core Lehmann (1936). The second half of the 20th century was marked mostly by the refinement of spherical Earth models Dziewonski et al. (1975). The next step to improve the model of the Earth was to introduce a 3D Earth model. Aki et al. (1977) used teleseismic data in a linearised tomography for regional 3D structure. Most conclusions regarding the approximate 3D structure in the Earth including the asthenosphere are based on ray theory Cerveny (2005), for example the study by Bastow et al. (2008) on upper mantle seismic structure beneath the Ethiopian hot spot. However the assumptions made in ray theory are only valid for smooth 3D heterogeneities that have a much larger scale

length than the dominant wavelength Spetzler et al. (2001); Williamson (1991). This limits the resolution of the models obtainable. With the goal in mind of a high resolution 3D Earth model an alternative to ray theory had to be found. This is where Full Waveform Inversion comes in. FWI seeks to move the frontier of what is achievable in terms of high resolution Earth models. Its development started in the late 1970s/early 1980s Bamberger et al. (1982); Tarantola (1984, 1986); Igel et al. (1996); Pratt et al. (1998) and still continues in more recent times Fichtner et al. (2008). The goal of this study is to build upon previous works, to evolve from the still frequently used 1D radially symmetric PREM model Dziewonski and Anderson (1981), towards a high resolution 3D Earth model. FWI can help to achieve this.

Full waveform inversion is a method that comes in several variations. A common element that always comes back, is that waves are simulated through an Earth model and discrepancies between simulated and recorded waves are reduced by adjusting model parameters. In each of these common steps several variations exist. In this chapter it should become clear to the reader how these steps were performed for this study and why.

3-1-1 Inversion Basics

The basic concept of inversion starts with the mathematical reasoning that if a physical system is understood, it should be possible to predict the data $\mathbf{d}$ given a set of physical equations g and a model $\mathbf{m}$ as in equation:

$$g(\mathbf{m}) = \mathbf{d} \tag{3-1}$$

Here model $\mathbf{m}$ could for example represent a model of the seismic velocities within the Earth. Data $\mathbf{d}$ could represent the recordings made by a seismometer. In many scientific areas forward modelling with a well known model is common. Modelling the airflow around an airplane is a typical example. In Earth sciences however the situation is quite the opposite. The behavior of the waves is understood very well but the medium through which the waves travel is often poorly known. This is where the inverse problem starts. Is it possible to turn the problem around and based on the physical relations g and data $\mathbf{d}$ find a model $\mathbf{m}$ that would explain the given data set $\mathbf{d}$? As in equation:

$$\mathbf{m} = g^{-1}\mathbf{d} \tag{3-2}$$

The equation looks quite trivial but the reality is more difficult. For a start, there is no such thing as an exact measured data set. Data is measured at regular or irregular intervals and always contains some noise. The noise could stem for example from imperfections of the measurement device or outside disturbances. Another challenge is that the wave equation has a unique solution given an elastic medium, but a band-limited dataset can be fit equally well by many models. Luckily there are strategies to mitigate these issues and come up with meaningful results that help to get a better understanding of the Earth. For now a good starting point in the quest to solve the inverse problem is to solve the forward problem first.

3-2 The Forward Problem

As mentioned in the previous section FWI relies on the accurate solution of the forward problem as in equation 3-1. To be able to solve the forward problem one needs to know how waves propagate. Fortunately, the physics of low–strain wave propagation call only for linear elastic relationships, which can be solved in a variety of ways. In this section the governing equations that form the basis of all wave propagation solvers are briefly discussed. Finally one needs a preferably good initial model as a starting point for the FWI process. In this section all of these aspects will be explained.

3-2-1 Governing Equations

The propagation of seismic waves through a medium can be modelled with help of the *elastic wave equation* (3-3) as in Tsvankin (2012). The equation is given using the Einstein summation convention Einstein (1916):

$$\rho \frac{\partial^2 u_i}{\partial t^2} - \frac{\partial \tau_{ij}}{\partial x_j} = f_i \tag{3-3}$$

where ρ is the density, $\mathbf{u} = (u_1, u_2, u_3)$ is the displacement vector, $\mathbf{f} = (f_1, f_2, f_3)$ is the (external) body force per unit volume, t is time and x_i are the Cartesian coordinates. A detailed derivation of the elastic wave equation can be found in Aki and Richards (2002). For a medium with a given density distribution and known applied body forces, equation 3-3 still contains two unknowns: the displacement field and the stress tensor τ_{ij}. To be able to solve equation 3-3 for displacement u it needs to be further constrained. When the amount of strain is small, the stress–strain relationship is linear and is described by the generalized Hooke's law Tsvankin (2012):

$$\tau_{ij} = c_{ijkl} \epsilon_{kl} \tag{3-4}$$

This relation is sufficiently accurate for most applications in seismic wave propagation. Here c_{ijkl} is the fourth order stiffness tensor, which includes the material properties and ϵ_{kl} is the strain tensor which is defined as:

$$\epsilon_{kl} = \frac{1}{2} \left(\frac{\partial u_k}{\partial x_l} + \frac{\partial u_l}{\partial x_k} \right) \tag{3-5}$$

Substituting equation 3-4 and 3-5 in 3-3 we find:

$$\rho \frac{\partial^2 u_i}{\partial t^2} - \frac{\partial}{\partial x_j} \left(c_{ijkl} \frac{\partial u_k}{\partial x_l} \right) \tag{3-6}$$

Equation 3-6 is valid for linearly elastic, anisotropic media. A regular fourth order tensor would have 81 components. Due to symmetry of the stress and strain tensors as in equation 3-7 and due to thermodynamic properties as described in Aki and Richards (2002), the following relations hold:

$$c_{ijkl} = c_{jikl} \tag{3-7}$$

$$c_{ijkl} = c_{klij} \tag{3-8}$$

These symmetries bring the number of unique stiffness elements down from 81 to 21. By using Voigt notation the fourth order stiffness tensor can be represented as a 6×6 matrix. This most general case with anisotropy in every direction, is called *triclinic*:

$$\mathbf{c^{(trc)}} = \begin{pmatrix} c_{11} & c_{12} & c_{13} & c_{14} & c_{15} & c_{16} \\ c_{12} & c_{22} & c_{23} & c_{24} & c_{25} & c_{26} \\ c_{13} & c_{23} & c_{33} & c_{34} & c_{35} & c_{36} \\ c_{14} & c_{24} & c_{34} & c_{44} & c_{45} & c_{46} \\ c_{15} & c_{25} & c_{35} & c_{45} & c_{55} & c_{56} \\ c_{16} & c_{26} & c_{36} & c_{46} & c_{56} & c_{66} \end{pmatrix} \tag{3-9}$$

Since there are often symmetries in the crystalline structure of a medium the most general case can be further simplified in several special cases. For this thesis, we will make the assumption that the underlying medium is transversely isotropic. In transversely isotropic media with a vertical symmetry axis (VTI), the stiffness tensor further simplifies as in Tsvankin (2012) to:

$$\mathbf{c^{(VTI)}} = \begin{pmatrix} c_{11} & c_{11} - 2c_{66} & c_{13} & 0 & 0 & 0 \\ c_{11} - 2c_{66} & c_{11} & c_{13} & 0 & 0 & 0 \\ c_{13} & c_{13} & c_{33} & 0 & 0 & 0 \\ 0 & 0 & 0 & c_{55} & 0 & 0 \\ 0 & 0 & 0 & 0 & c_{55} & 0 \\ 0 & 0 & 0 & 0 & 0 & c_{66} \end{pmatrix} \tag{3-10}$$

Where the stiffness constants and density can be related to the following seismic velocities:

$$v_{PH} = \sqrt{\frac{c_{11}}{\rho}}, \quad v_{PV} = \sqrt{\frac{c_{33}}{\rho}}, \quad v_{SH} = \sqrt{\frac{c_{66}}{\rho}}, \quad v_{SV} = \sqrt{\frac{c_{55}}{\rho}} \tag{3-11}$$

and the anisotropy parameter η is defined as in Dziewonski and Anderson (1981):

$$\eta = \frac{c_{13}}{c_{11} - 2c_{55}} \tag{3-12}$$

For the isotropic case the stiffness tensor can be further simplified:

$$\mathbf{c^{(iso)}} = \begin{pmatrix} c_{33} & c_{12} & c_{12} & 0 & 0 & 0 \\ c_{12} & c_{33} & c_{12} & 0 & 0 & 0 \\ c_{12} & c_{12} & c_{33} & 0 & 0 & 0 \\ 0 & 0 & 0 & c_{55} & 0 & 0 \\ 0 & 0 & 0 & 0 & c_{55} & 0 \\ 0 & 0 & 0 & 0 & 0 & c_{55} \end{pmatrix} \tag{3-13}$$

With

$$c_{12} = \lambda = c_{33} - 2c_{55}, \quad c_{55} = \mu \quad \text{and} \quad c_{33} = K + \frac{4}{3}\mu \tag{3-14}$$

Where μ is the shear modulus and K is the bulk modulus. Using the Lamé parameters λ and μ the stiffness tensor for the isotropic case can be expressed with just two elements:

$$\mathbf{c}^{(\mathbf{iso})} = \begin{pmatrix} \lambda+2\mu & \lambda & \lambda & 0 & 0 & 0 \\ \lambda & \lambda+2\mu & \lambda & 0 & 0 & 0 \\ \lambda & \lambda & \lambda+2\mu & 0 & 0 & 0 \\ 0 & 0 & 0 & \mu & 0 & 0 \\ 0 & 0 & 0 & 0 & \mu & 0 \\ 0 & 0 & 0 & 0 & 0 & \mu \end{pmatrix} \tag{3-15}$$

Substituting 3-15 into the elastic wave equation 3-6 we obtain the equation of motion for homogeneous isotropic media:

$$\rho \frac{\partial^2 u_i}{\partial t^2} - (\lambda+\mu)\frac{\partial^2 u_j}{\partial x_i \partial x_j} - \mu \frac{\partial^2 u_i}{\partial x_j \partial x_j} = f_i \tag{3-16}$$

These simplifying cases of the elastic wave equation can prove very useful in the modelling of seismic waves. They reduce the computational cost of modelling, because there will be less multiplications involved. These assumptions also act as an injection of a priori information into the inverse problem, reducing the number of model parameters at the cost of rather strong assumptions on the elastic medium.

3-2-2 Solver: SPECFEM3D_GLOBE

Since analytical solutions to the wave equation only exist for relatively simple models and Earth is highly complex, the wave equation needs to be solved numerically. This means that the wavefield will need to be discretized in space and time. Depending on the numerical method applied, the wavefield coefficients could represent discrete values of $\mathbf{u}(\mathbf{x}, t)$ as in finite differences or polynomial coefficients when the wavefield is approximated by a polynomial, as in finite elements. Following the discretization of the displacement formulation as in equation 3-6, each element is represented by a local system of equations. In the case of the spectral element method this local system of equations satisfies the wave equation, where the displacement field u is approximated by a polynomial. The local systems of equations can be combined into a global system of equations:

$$\mathbf{M}^{global} \cdot \ddot{\mathbf{u}}^{global}(t) + \mathbf{K}^{global} \cdot \mathbf{u}^{global}(t) = \mathbf{f}^{global}(t) \tag{3-17}$$

With $\mathbf{M}$ representing the *mass matrix*, which includes all the values of ρ and $\mathbf{K}$ representing the *stiffness matrix*, which contains all the stiffness coefficients from the previously described fourth order stiffness tensor. For more information on how the global system of equations is composed, the reader is referred to Fichtner (2010).

To model the earthquake waves, the global wave propagation solver SPECFEM3D_GLOBE Spe (2016a) is used. SPECFEM3D_GLOBE simulates global and regional seismic wave propagation. It includes effects due to 3D variations in shear-wave speed, density and compressional-wave speed. It also accounts for the effects related to ellipticity, topography, bathymetry, the oceans, Earth's rotation and self-gravitation. More details on the inner workings of the solver can be found in Komatitsch and Tromp (2002a,b). The software can be downloaded from GitHub Spe (2016b).

An important reason to choose SPECFEM_GLOBE as modelling software is because it is a highly optimized solver. The solver uses the spectral element method to solve for the forward wavefield. The spectral element was originally developed for fluid mechanics Patera (1984) and has two clear advantages: When Lagrange polynomials collocated at the Gauss–Lobatto–Legendre (GLL) points are used in combination with GLL quadrature, the mass matrix $\mathbf{M}$ becomes *diagonal* and can be trivially inverted. This makes it easy to obtain an explicit expression for $\ddot{\mathbf{u}}^{global}(t)$:

$$\ddot{\mathbf{u}}^{global}(t) = \mathbf{M}^{global\,-1} \cdot \left[\mathbf{f}^{global}(t) - \mathbf{K}^{global} \cdot \mathbf{u}^{global}(t)\right] \tag{3-18}$$

To take full advantage of the fact that the global mass matrix is diagonal, time discretization of 3-18 is achieved, based upon a classical explicit second-order finite-difference scheme. Another key advantage is that the free surface boundary conditions are implicitly satisfied within the weak form of the wave equation. For a derivation, please refer to Fichtner (2010). This in contrast to finite-difference methods, where they need to be treated explicitly, which can be a challenging task. Another benefit of SPECFEM3D_GLOBE is that since version 7.0 it offers GPU support which helps to speed up tasks that can be done in parallel Komatitsch et al. (2010). This greatly reduces the wall clock time required to solve the forward problem. These characteristics result in a solver that is both very accurate and fast. The efficiency of the solver allows the use of higher frequencies in the inversion, which can result in a higher resolution image. The solver will be running on the Piz Daint dai (2016) supercomputer at the Swiss National Supercomputing Center (CNCS) in Lugano. The parameters used by the solver can be found in Appendix B.

3-2-3 Initial model

Before a first forward wave field can be modelled an initial model of the Earth is required. A good initial model is crucial in most non-linear inverse problems. To reach the global minimum it is required that the initial model matches the observations within less then half a period at the desired frequency Pratt (1999). This prevents getting stuck in a local minimum. For this study the Collaborative Seismic Earth Model (CSEM) Afanasiev et al. (2016) was used as a starting model. The CSEM is a computational framework which enables the combination of local and global seismic data into a consistent model, describing Earth's structure on all seismically accessible scales. The background velocity of the CSEM is based on the 1D PREM Dziewonski and Anderson (1981). Added to this are the 3D S-velocity perturbations from S20RTS Ritsema et al. (1999). The initial crustal model is the model by Meier et al. (2007b,a). Within the region of the CSEM that will be used in this study, higher resolution submodels have been incorporated already in the South Atlantic Colli et al. (2013) and Europe Fichtner et al. (2013a,b). Spherical slices at 200 km depth from v_{SV} and v_{SH} are shown in Figure 3-1.

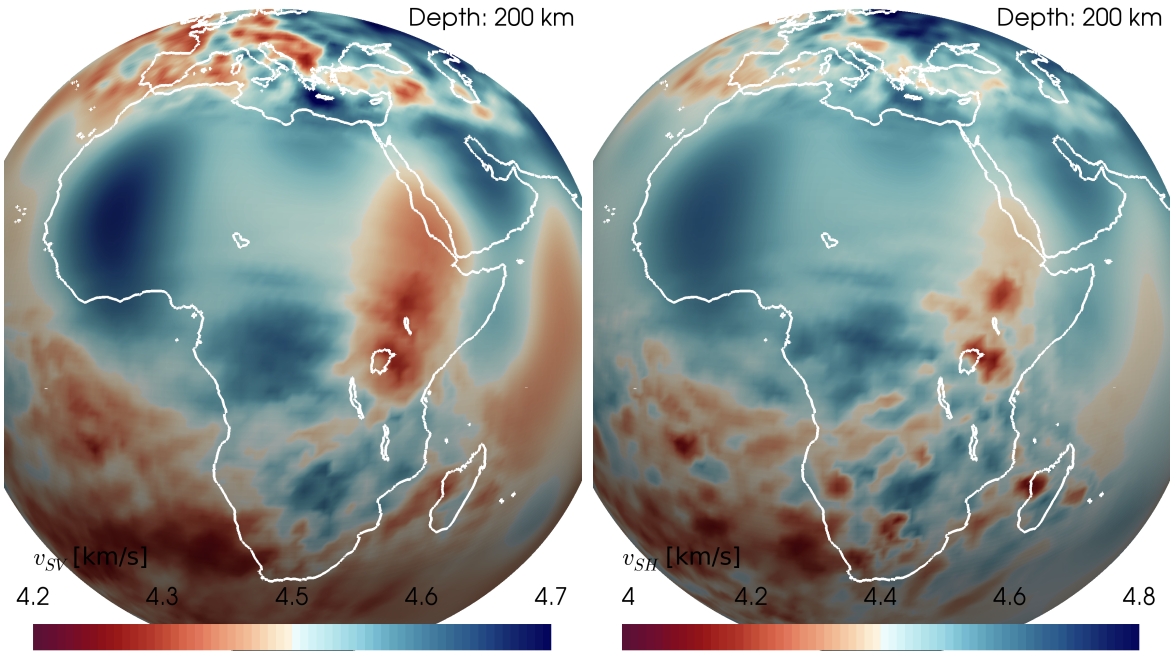

(a) v_{SV} **(b)** v_{SH}

Figure 3-1: Spherical slice through the v_{SV} (left) and v_{SH} (right) model at 200 km depth in the initial model.

Solving the wave fields for the earthquake events results in the first synthetic data. The acquired synthetic data depends on the solver and the model of the Earth. The goal of inversion is to find a model that creates synthetics that represent the recorded data as to within the noise. Since the regional simulation option of SPECFEM3D_GLOBE is used, the model only extends down to the outer core. Modelling the Aegean sea earthquake on August 1st, 2014 results in the synthetic trace shown in Figure 3-2. This trace is bandpass filtered again to filter the waves between 40 seconds and 100 seconds.

3-3 The Adjoint Method

The tomographic inversion in this study attempts to solve the deterministic inverse problem as opposed to probabilistic inverse problem. This means finding the one model that best describes the measured data. The ultimate goal would be to find the Earth model $\mathbf{m}$ that is as close as it can get to the true Earth. In this case one could expect that the recorded displacement field $\mathbf{u}^0$ is very close to the modelled synthetic data $\mathbf{u}(\mathbf{m})$. Note here that the superscript 0 is used to make the distinction between the recorded wave field and the synthetic wave field. In reality one should not pursue to perfectly match synthetic data with the recorded data, because the synthetic data remains an approximation and a perfect match would imply that noise is also fit.

To measure how well the data is predicted by the model, a misfit functional $\chi(\mathbf{m})$ is defined which compares the observed wave field $\mathbf{u}^0$ with the predicted wave field $\mathbf{u}(\mathbf{m})$. The goal is to find an optimal physically reasonable Earth model $\widetilde{\mathbf{m}}$ that minimizes this misfit function.

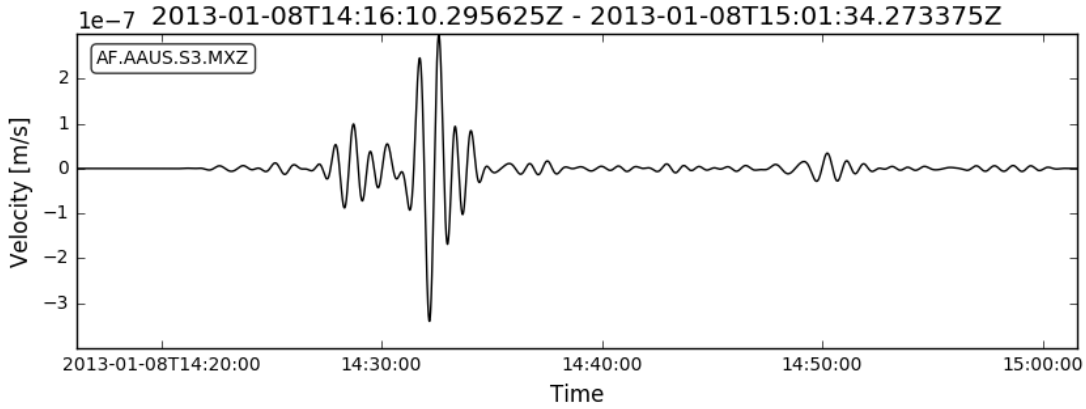

Figure 3-2: Synthetic data after processing with the same bandpass filter applied as to the preprocessed recorded data. As in Figure 2-5, station AAUS from the Africa Array is used and the modelled earthquake is GCMT event Aegean Sea Mag 5.8 2013-1-8-14.

In our case the model consists of:

$$\mathbf{m}(\mathbf{x}) = [v_{PV}(\mathbf{x}), v_{PH}(\mathbf{x}), v_{SV}(\mathbf{x}), v_{SH}(\mathbf{x}), \rho(\mathbf{x}), \eta(\mathbf{x})] \tag{3-19}$$

Where v_{PV} and v_{PH} are the vertical and horizontally polarised compressional wave velocities, v_{SV} and v_{SH} are the vertically and horizontally polarised shear wave velocities, ρ is the density and η is an a parameter governing anisotropy as defined by Dziewonski and Anderson (1981). Because $\chi(\mathbf{m})$ is in general a very complicated and non-linear function of $\mathbf{m}$, the optimal model $\widetilde{\mathbf{m}}$ is approximated with an iterative minimisation technique, where a successive model $\mathbf{m}_{i+1}$ explains the recorded data $\mathbf{u}^0$ better than the previous model $\mathbf{m}_i$. Model updates are of the form:

$$\mathbf{m}_{i+1} = \mathbf{m}_i + \gamma_i \mathbf{h}_i \quad \text{with} \quad \chi(\mathbf{m}_{i+1}) < \chi(\mathbf{m}_i) \tag{3-20}$$

Where $\mathbf{h}_i$ is the descent direction and γ_i is the step length. With the general descent method the descent direction for the first update is defined as:

$$\mathbf{h}_0 = -\nabla_m \chi(\mathbf{m}_0) \tag{3-21}$$

Where $\nabla_m \chi(\mathbf{m}_0)$ represents the gradient with respect to the model parameters. The response of the misfit function to a small change in the model parameter $\mathbf{m}+\epsilon\delta\mathbf{m}$ can be approximated with the following equation:

$$\nabla_m \chi(\mathbf{m})\delta\mathbf{m} = \lim_{\epsilon \to 0} \frac{1}{\epsilon} [\chi(\mathbf{m} + \epsilon\delta\mathbf{m}) - \chi(\mathbf{m})] \tag{3-22}$$

However in many problems the number of model parameters is very large and the forward simulation required to evaluate the misfit of the slightly perturbed model is computationally

expensive. This makes the finite difference approximation of equation 3-22 so expensive, that it is not feasible any more to evaluate it for larger problems. This is where the adjoint method comes in. The adjoint method greatly reduces the computational cost required to obtain the gradient of the misfit functional with respect to the model parameters.

Consider an observable wave field $\mathbf{u}$ that depends on the model parameters $\mathbf{m} \in \mathfrak{M}$, the position $\mathbf{x} \in G \subset \mathbb{R}^3$ and time $t \in T = [t_0, t_1]$:

$$\mathbf{u} = \mathbf{u}(\mathbf{m}; \mathbf{x}, t) \tag{3-23}$$

Where $\mathfrak{M}$ indicates the model space and the semicolon indicates that $\mathbf{u}$ evolves both in space and time. In seismology the elastic wave field is linked to the forces via the wave equation 3-6 to external sources $\mathbf{f}$ and model parameters $\mathbf{m}$. This relation can be written as:

$$\mathbf{L}(\mathbf{u}, \mathbf{m}) = \mathbf{f} \tag{3-24}$$

Equation 3-24 is known as the forward problem, where $\mathbf{L}$ represents the physical theory that links the external forces and model to the elastic wavefield. In inversion however our main interest is not the wavefield $\mathbf{u}$ but the outcome of the objective functional $\chi(\mathbf{m})$. There exist several types of objective functionals, each with their own applications, but for this formulation of the adjoint equation we will stick to a general of the objective functional:

$$\chi(\mathbf{m}) = \int_T \int_G \chi_1 \left[\mathbf{u}(\mathbf{m}; \mathbf{x}, t)\right] \mathrm{d}t \, \mathrm{d}^3\mathbf{x} = \langle \chi_1(\mathbf{m}) \rangle \tag{3-25}$$

Where $\langle . \rangle$ is a short notation for the integral over $T \times G$. The derivative of $\chi[\mathbf{u}(\mathbf{m})]$ with respect the model parameters $\mathbf{m}$ in the direction of $\delta\mathbf{m}$ follows from the chain rule:

$$\nabla_m \chi \, \delta\mathbf{m} = \nabla_u \chi \, \delta\mathbf{u} = \langle \nabla_u \chi_1 \, \delta\mathbf{u} \rangle \tag{3-26}$$

Where

$$\delta\mathbf{u} := \nabla_m \mathbf{u} \, \delta\mathbf{m} \tag{3-27}$$

Note that equation 3-26 is equal to equation 3-22. The difficulty with this equation is as mentioned before that $\nabla_m \chi(\mathbf{m})$ is difficult to approximate because a forward run is required for each model perturbation. To be able to compute the gradient of the objective functional $\nabla_m \chi(\mathbf{m})$ we need to remove $\delta\mathbf{u}$ in equation 3-26. For this purpose we differentiate the theoretical relationship of the forward problem of equation 3-24. Using the chain rule we get:

$$\nabla_m \mathbf{L} \, \delta\mathbf{m} + \nabla_u \mathbf{L} \, \delta\mathbf{u} = 0 \tag{3-28}$$

Here the force term $\mathbf{f}$ disappeared because it is independent of the model parameters $\mathbf{m}$. Multiplying equation 3-28 with a test function $\mathbf{u}^\dagger$ and applying the integral over $T \times G$ in short notation gives:

$$\langle \mathbf{u}^\dagger \cdot \nabla_m \mathbf{L} \, \delta\mathbf{m} \rangle + \langle \mathbf{u}^\dagger \cdot \nabla_u \mathbf{L} \, \delta\mathbf{u} \rangle = 0 \tag{3-29}$$

Adding 3-26 and equation 3-29 results in:

$$\nabla_m \chi \, \delta \mathbf{m} = \langle \nabla_u \chi_1 \, \delta \mathbf{u} \rangle + \langle \mathbf{u}^\dagger \cdot \nabla_u \mathbf{L} \, \delta \mathbf{u} \rangle + \langle \mathbf{u}^\dagger \cdot \nabla_m \mathbf{L} \, \delta \mathbf{m} \rangle \tag{3-30}$$

Rewriting using adjoint operators $\nabla_u \chi_1{}^\dagger$ and $\nabla_u \mathbf{L}^\dagger$ which are defined as:

$$\langle \nabla_u \chi_1 \, \delta \mathbf{u} \rangle = \langle \delta \mathbf{u} \cdot \nabla_u \chi_1{}^\dagger \rangle \tag{3-31}$$

and

$$\langle \mathbf{u}^\dagger \cdot \nabla_u \mathbf{L} \, \delta \mathbf{u} \rangle = \langle \delta \mathbf{u} \cdot \nabla_u \mathbf{L}^\dagger \mathbf{u}^\dagger \rangle \tag{3-32}$$

We then arrive at equation:

$$\nabla_m \chi \, \delta \mathbf{m} = \langle \delta \mathbf{u} \cdot (\nabla_u \chi_1{}^\dagger + \nabla_u \mathbf{L}^\dagger \mathbf{u}^\dagger) \rangle + \langle \mathbf{u}^\dagger \cdot \nabla_m \mathbf{L} \, \delta \mathbf{m} \rangle \tag{3-33}$$

which is valid for any $\mathbf{u}^\dagger$ and $\delta \mathbf{u}$. We can now eliminate $\delta \mathbf{u}$ if we determine a field $\mathbf{u}^\dagger$ which satisfies the equation:

$$\nabla_u \mathbf{L}^\dagger \mathbf{u}^\dagger = -\nabla_u \chi_1{}^\dagger \tag{3-34}$$

Equation 3-34 is called the adjoint equation, where $\mathbf{u}^\dagger$ and $-\nabla_u \chi_1{}^\dagger$ are the *adjoint field* and *adjoint source*, respectively. When the adjoint field is found then equation 3-33 simplifies to:

$$\nabla_m \chi \, \delta \mathbf{m} = \langle \mathbf{u}^\dagger \cdot \nabla_m \mathbf{L} \, \delta \mathbf{m} \rangle \tag{3-35}$$

Now $\nabla_m \chi \, \delta \mathbf{m}$ can be computed without the explicit knowledge of $\delta \mathbf{u}$. However we do have to find the adjoint operator $\nabla_u \mathbf{L}^\dagger$ and a solution to the adjoint equation 3-34.

Fréchet kernels are defined as the volumetric densities of the Fréchet derivative $\nabla_m \chi(\mathbf{m})$:

$$K_m \equiv \frac{\mathrm{d}}{\mathrm{d}V} \nabla_m \chi = \int_T \mathbf{u}^\dagger \cdot \nabla_m \mathbf{L} \, \mathrm{d}t \tag{3-36}$$

The Fréchet kernels show how a change in the model parameters at a certain position $\mathbf{x}$ influences the total misfit functional. In other terms, it maps misfit values in data space to perturbations in model space. Thereby it greatly increases our understanding of the physical causes that influence the misfit. Kernels give an understanding of how the model gets updated to decrease the misfit. The derivative of the objective functional can now be written as:

$$\nabla_m \chi \delta \mathbf{m} = \langle \mathbf{u}^\dagger \cdot \nabla_m \mathbf{L} \, \delta \mathbf{m} \rangle = \int_G K_m \, \delta \mathbf{m} \, \mathrm{d}^3 \mathbf{x} \tag{3-37}$$

3-3-1 Misfits

In the previous section we used a general formulation of the misfit functional $\chi(\mathbf{m})$. There exist several methods to define the misfit. The choice for a certain method should be such that the waveform information can be exploited as good as possible Brossier et al. (2010). This depends on the quality of the initial model, the modelling tools used and the data that is available. The classical way to define the misfit is the L_2 distance Bamberger et al. (1982). This compares the measured and predicted wave fields at each point in time and takes the squared distance in amplitude. Intuitively, this can be linked to the Born approximation, but the method can be quite problematic. The misfit functional will have many local minima because as you change the model and shift the synthetics forward or backwards in time you increase and decrease the misfit depending on the dominant phase differences. The L_2 distance method thus already requires a high quality initial model. Even when the initial model is very good, outliers in the data can have significant unwanted effects. In this study the amplitude data is not reliable and is not used, chiefly because amplitude can vary dramatically from station to station, due to instrument responses and un-modelled site effects. Fortunately there exist other methods. A better option for our case is cross-correlation time shifts Gee and Jordan (1992); Zhou et al. (1995). The optimal cross-correlation time shift is defined as the time where the cross-correlation between observed and predicted data reaches its global maximum. It thus relies on phase differences instead of amplitudes. The applicability of the cross-correlation time shift is limited to situations where single phases are clearly separable and where observed and synthetic waveforms are similar. The type of misfit used in this study is the *time-frequency phase misfit* Fichtner et al. (2008); Kristeková et al. (2009) and has been used before in waveform inversions on continental scales Fichtner et al. (2009). It is defined as:

$$\chi_p{}^2(u_i{}^0, u_i) := \int_{\mathbb{R}^2} W_p{}^2(t,\omega)[\phi_i(t,\omega) - \phi_i{}^0(t,\omega)]^2 \mathrm{d}t\,\mathrm{d}\omega \tag{3-38}$$

Where W_p is the positive weighting function and $\Delta\phi_i = \phi_i - \phi_i{}^0$ is the phase difference. Where ϕ_i represents the modelled phase and $\phi_i{}^0$ represents the recorded phase. The phase difference can be interpreted as a time shift at a certain frequency. The weighting function helps to only include phase differences in the meaningful frequency range. For example when it is known that noise makes up a large part energy at a certain frequency range, the weighting can help reduce its influence in the calculation of the misfit. An advantage for this study is that time-frequency misfit relax the requirements of waveform similarity compared to cross-correlation time shifts Fichtner (2010). Another key benefit is the ability to exploit information from complete wave trains even when seismic phases are interfering, which happens especially at short epicentral distances. In the data set used in this study, there is mixture of epicentral data available. Using time-frequency misfits thus make sure that a larger amount of this data can be used effectively.

3-3-2 Window selection

With the processed recorded data and synthetic data in place another step needs to be performed. That is selecting the time windows for which meaningful misfits will be calculated. Except for limited synthetic examples, often only parts of the seismograms are used.

More often than not seismometers are malfunctioning or other sources of noise result in bad recordings. Historically one would look through the seismograms and only select the good parts of the seismograms. In this study this would mean looking at 11297 seismograms for every iteration. Fortunately this process can be automated by using an automatic window selection tool, such as is available in LASIF Krischer et al. (2015a). This tool was used to select windows, based upon the similarity between synthetic and recorded data. This not only prevents incorrect data from forcing the inversion into the wrong direction, but also helps to make sure that the inversion does not get stuck in a local minimum. As mentioned before, the risk of getting stuck in a local mininum greatly increases, when the phase differences between synthetic and recorded data are larger than half a wavelength. In Figure 3-3, the selected windows are visualised with grey shaded backgrounds.

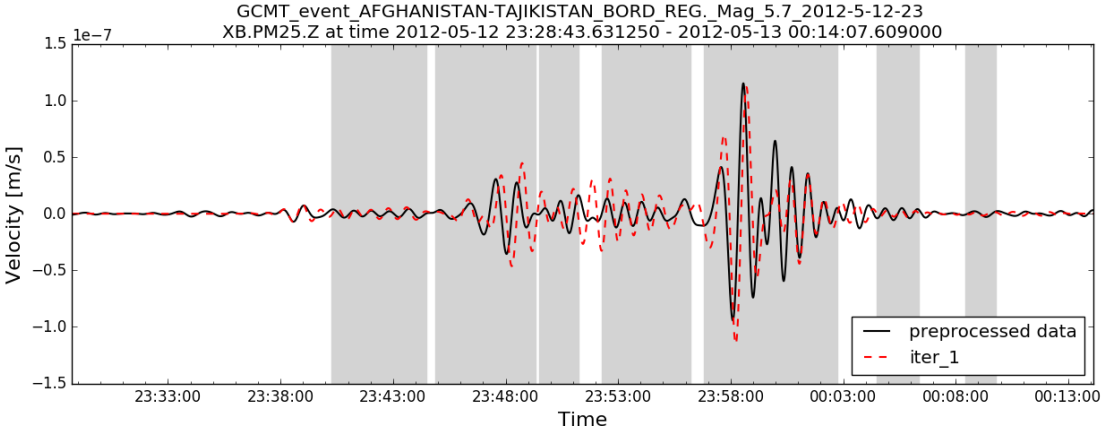

Figure 3-3: An illustration of the windows selected by LASIF Krischer et al. (2015a), selected windows have a grey background.

3-3-3 Creating Adjoint sources

With a definition of the misfit present and windows selected it is time to generate the adjoint sources. The definition of the adjoint sources follows from the objective function used. The definition of the objective functional 3-25 with the time-frequency phase misfit can now be written as:

$$\nabla_m \chi_p \, \delta\mathbf{m} = \frac{1}{\chi_p} \int_{\mathbb{R}^2} {W_p}^2 (\phi_i - {\phi_i}^0)(\nabla_m \phi_i \, \delta\mathbf{m}) \, \mathrm{d}t \, \mathrm{d}\omega \tag{3-39}$$

The adjoint source that corresponds to the time-frequency phase misfit as defined in Fichtner (2010) is now:

$$\mathbf{f}^\dagger(\mathbf{x}, t) = \frac{1}{\chi_p} \Im\mathfrak{m} \, {F_h}^{-1} \left[\mathcal{P}\tilde{u}_i\right](t) \, \mathbf{e}_i \, \delta(\mathbf{x} - \mathbf{x}^r) \tag{3-40}$$

Where ${F_h}^-1$ denotes the inverse time-frequency transform, $\mathbf{x}^r$ is the receiver location from which the adjoint source is constructed and $\mathcal{P}$ is used for lighter notation and is defined as:

$$\mathcal{P}(t,\omega) := \frac{{W_p}^2(t,\omega)}{|\tilde{u}_i(t,\omega)|^2}\left[\phi_i(t,\omega) - {\phi_i}^0(t,\omega)\right] \tag{3-41}$$

Kernels are generated from the interaction between the forward wavefield **u** and the adjoint wavefield that follows from the adjoint sources defined at the receiver locations. The interaction field that forms the kernel can be thought of as propagating from the receiver to the source in reverse time Tromp et al. (2005).

3-3-4 Kernel Simulation

The previous steps were taken to allow us to generate a first kernel. The kernel represents a volume density of the gradient of the objective functional with respect to the model parameters. To construct the kernel SPECFEM3D_GLOBE was used. In Figure 3-4a the raw v_{SV} kernel is shown at a depth of 100 km. The raw kernel shows a lot of detail on the gradient but unfortunately we cannot be so sure this kernel is really pointing in the direction of the optimal model. Kernel values are calculated on the numerical grid of the solver, which includes ten Gauss Lobatto Legendre (GLL) points per wavelength. This is strongly over resolved. The kernels are smoothed to ensure that updates are more in line with what is expected physically: resolution on about the scale of a wavelength. To give an idea, for S-waves with a velocity of approximately 5 km/s and periods of 40 s the wavelength is 200 km.

Measurement or modelling errors also find their way into the kernel and to be more certain that we will indeed update our initial model to a model that is closer to the optimal Earth model raw kernels are generally smoothed. The net effect is that the final model will be more conservative and the risk of overfitting the data is reduced. The smoothed v_{SV} kernel is shown in 3-4b. Now it becomes clear that there is much more sensitivity to the region, where there is a high density of rays as shown in Figure 2-4. In the next section a station weighting scheme will be introduced to reduce this effect.

3-4 Improving convergence: station weighting

To have a better intuitive understanding of kernels it is instructive to think of the most simple case when there is just one source and one receiver. In this case, for most seismic phases the kernel takes the form of a cigar shaped object, also known as the banana-doughnut kernel Tromp et al. (2005). This means that the objective function is sensitive to changes to the model within this range. In Figure 3-4b, two of those roughly cigar shaped are present in the region, where there is a lot of ray coverage, as in Figure 2-4. This happens because there is a relatively high amount of stations present in Southern Spain and Marocco, and events line up along the Southern Mid-Atlantic Ridge. Because of these circumstances updating with this gradient would mean only updating a small part of the region of interest. This means that in the current iteration the misfit is largely influenced by the model parameters in those regions. Thus update becomes more sensitive to the two cigars than to the rest of Africa. To reduce the effect of clustering on the sensitivity of the kernels a weighting scheme was introduced. Each of the stations is weighted based on a measure of clustering.

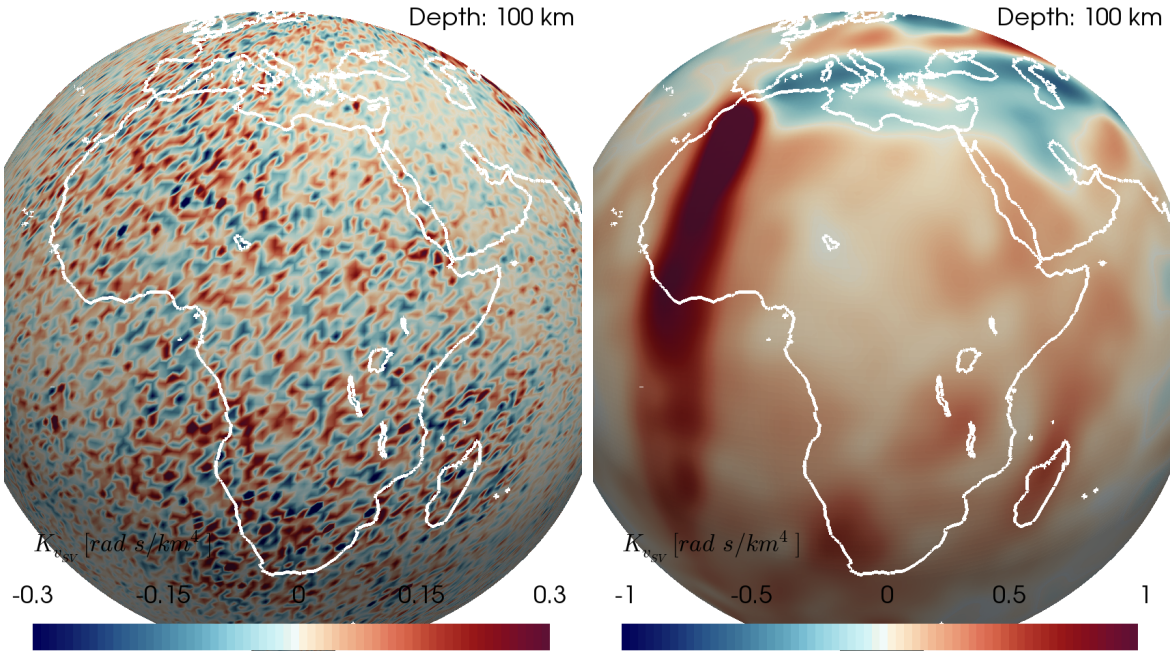

(a) Raw kernel **(b)** Smoothed kernel

Figure 3-4: Raw vs. smoothed kernel. The gaussian widths for smoothing are $\sigma_h = 250$ km, $\sigma_v = 5$ km.

$$\beta_a = \left(\sum_{i=1, i \neq a}^{n} \frac{1}{|\mathbf{x}_i - \mathbf{x}_a|} \right)^{-1} \tag{3-42}$$

The weight β_a assigned to any station is defined as in equation 3-42, where the distance $|\mathbf{x}_i - \mathbf{x}_a|$ is distance between the current station a and station i from the set of n stations, which are all the other stations. The adjoint sources are multiplied with the weighting factor β and the result can be seen in Figure 3-5. It shows a more balanced kernel. The same weighting factor is used to scale the magnitude of the misfit at all stations.

3-5 Model update

With the gradient of the misfit functional known it can be used to update the model as in equation 3-20. For the first iteration the gradient $\mathbf{h}_i$ is equal to the gradient of the misfit functional $\nabla_m \chi$. This way of updating is called the steepest descent method. The step length γ_i still needs to be found. This is done with a *line search* in the direction of the gradient.

3-5-1 Step length search

The step length search works with calculating the total misfit $\chi(\mathbf{m})$ for several model perturbations. Any small perturbation should normally decrease the misfit, but adding too large

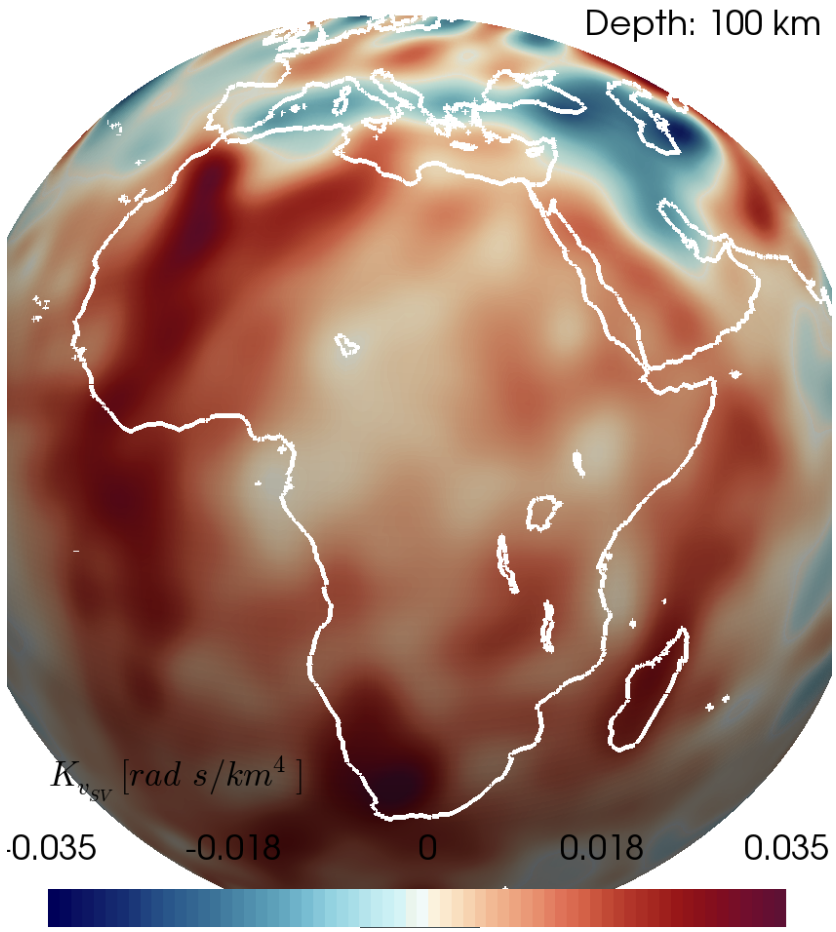

Figure 3-5: Spherical slice of the weighted V_{SV} kernel at 100 km depth.

updates to the model could lead to overshooting and physically unreasonable results. The goal of the step length search is to find the step length within a physically plausible range which most effectively reduces the misfit. To save on the costs of forward modelling only the twenty-five earthquake events with the largest misfits are evaluated. For the first iteration the misfit was evaluated for model updates with a maximum of 0%, 1.5% and 3% respectively. A parabola is fitted to connect the three points as can be seen in Figure 3-6. The step length at the expected minimum of the parabola will be used to update the model.

After performing one model update, as in equation 3-20, where $\mathbf{h}_i$ is the gradient of the first kernel, and with a step length that results in model updates with a maximum of 1.75 %, we began a new iteration with the updated model. New synthetics were generated from the updated. The synthetics moved slightly closer to the recorded data, as can be seen in Figure 3-7.

3-6 Results

After the first model update the entire process needs to be repeated to be able to converge to the model $\widetilde{\mathbf{m}}$, that corresponds to the global minimum of the misfit function $\chi(\mathbf{m})$. The entire

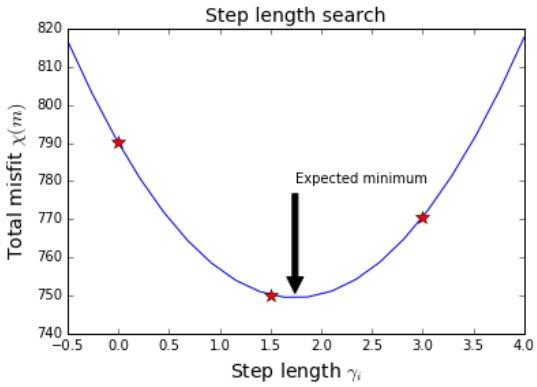

Figure 3-6: An example of a line search to find the optimal step length. The red stars represent the tested model perturbations. The blue line is the fitted parabola. The parabola shows a minimum at a model update of approximately 1.75 %.

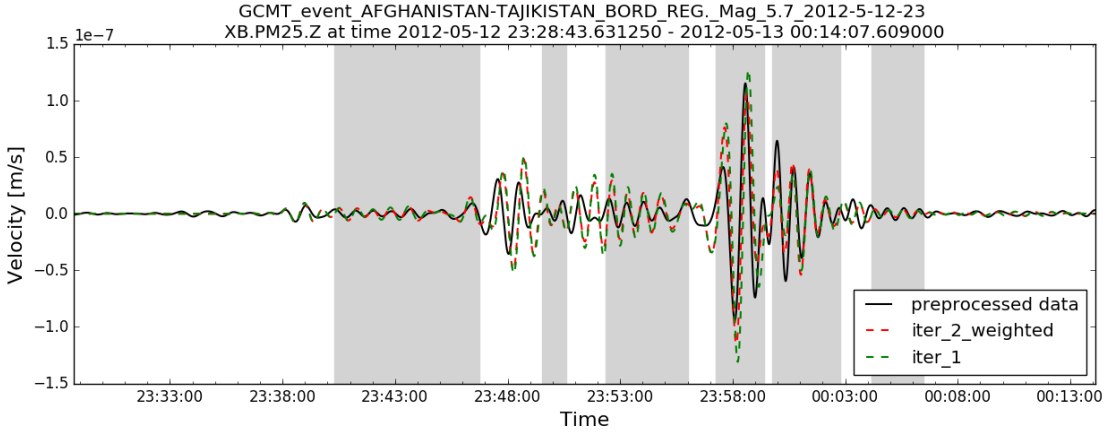

Figure 3-7: The synthetics generated after one model update show a slight improvement in data fit. This is the same earthquake as in Figure 3-3.

process starting from the forward modelling is repeated with the updated model as summarized in Figure 3-8. Each iteration generates its own synthetics and kernels. The following model updates were performed using the conjugate gradient method. This method helps to accelerate convergence towards the optimal model by using the gradient of the previous iteration to adjust the current gradient. In this results section the focus will be on showing the final model along with its synthetics and comparing it to the initial model. Challenges faced during the iterations will also be described as well as their solutions. Figure 3-9 shows the total misfit relative to the first calculated misfit after every performed model update, for the 25 events with the largest misfits.

As can be seen from Figure 3-9 misfits were decreasing rapidly for the first three updates, but convergence started to slow down after that. There are several possible explanations for this. The kernels were smoothed and perhaps because of oversmoothing, it became impossible to further reduce the misfit. Another possible explanation is that boundary artefacts started to appear near the boundary of the modelled domain.

The boundary effects, as seen in Figure 3-10 are caused by the imperfect paraxial boundary

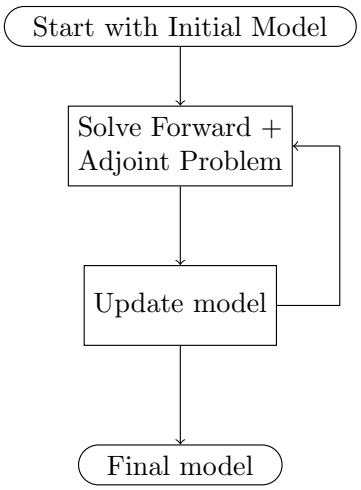

Figure 3-8: Flow chart that summarizes an iteration of the inversion process.

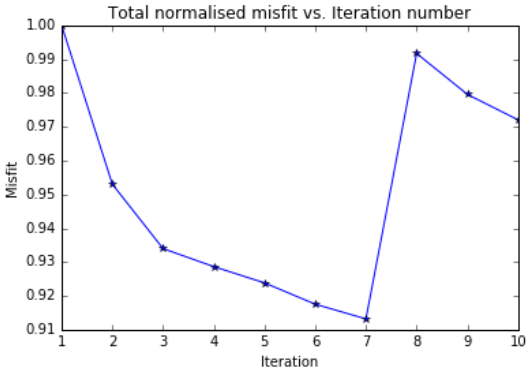

Figure 3-9: Misfit plot shows the total relative misfit over durations. Misfit increases between iteration 7 and 8 because additional windows were selected.

conditions, which are implemented in SPECFEM3D_GLOBE. The boundaries do not fully absorb the forward and adjoint wavefields. Apart from bringing artefacts into the Earth model near the boundaries of the model, this has another negative effect on the step length search. When a model update with a maximum perturbation of 2% is chosen and model updates are relative to the amplitude of the gradient this means that, for example a 2% update will only occur the region with the steepest gradients. Thus as can be seen from Figure 3-10, the model of Africa barely received substantial updates.

To solve this problem it was decided to taper off the kernels starting from an epicentral distance to the edge of the modelled domain of 25 degrees, and linearly tapering down the kernel amplitudes to 0 over 5 degrees of latitude or longitude. At iteration eight, windows were selected again. More windows were picked as a result of a better match between synthetics and preprocessed data. This is a stronger confirmation of an improved Earth model than just a reduction in the relative total misfit, because it means that data that was not previously used for the inversion is also showing a better match with the synthetics. Since the total length of selected windows increased, the length over which the misfit is calculated also increases. This results in a larger misfit value and explains why the total relative misfit can be seen to

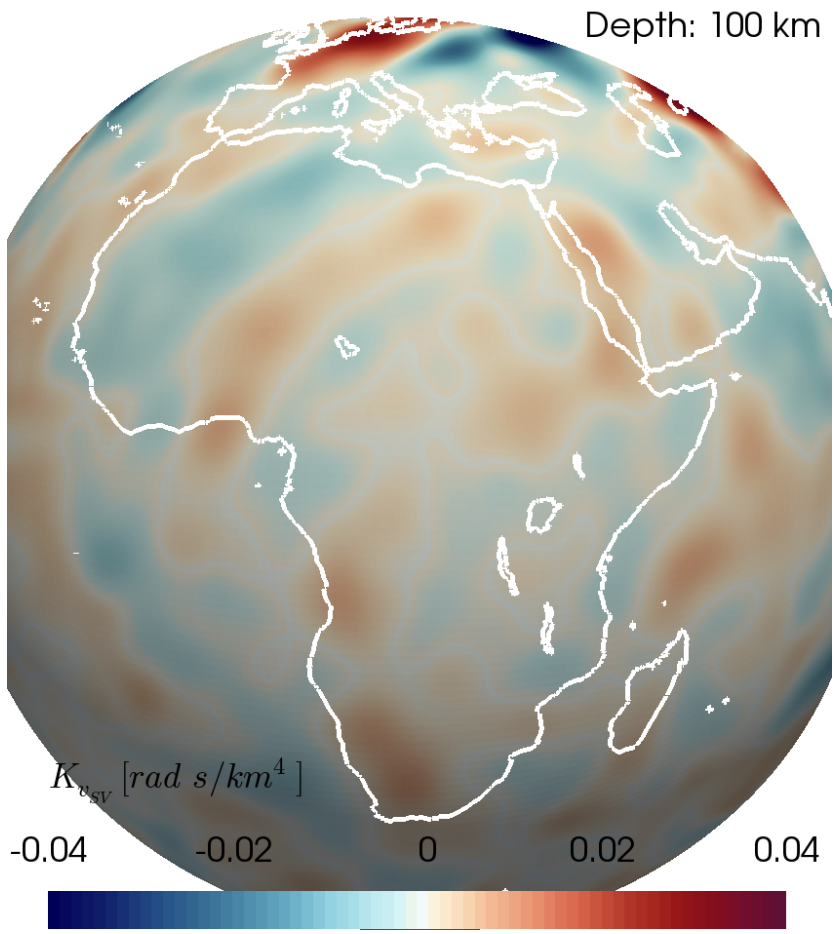

Figure 3-10: Spherical slice of the weighted v_{SV} kernel at iteration 7 at 100 km depth. Boundary artefacts show stronger amplitudes.

move back up. In iteration eight apart from selecting new windows and tapering the kernel on the edges of the domain, horizontal Gaussian smoothing was also reduced from σ_h of 250 km to 180 km. The resulting kernel can be seen in Figure 3-11.

Using the newly obtained kernel, the relative misfit started to reduce quicker again and a larger update was performed in the region of interest. Unfortunately due to time constraints this is were the inversion ends. Further model updates will likely bring the model closer to the optimal model. The seismic velocity that shows the biggest changes is v_{SV}, this is related to the fact that S-waves propagate slower and seismometers are better at measuring Rayleigh waves than Love waves, which results in more sensitivity to v_{SV}. In Figure 3-12 spherical slices of the initial and final v_{SV} model are shown at depths of 100 km and 200 km. In Figure 3-13 more spherical slices are shown at a depth of 300 km and 400 km. Model updates are smooth of nature because of the smoothing applied to the kernels. The contours of the West-African craton seem to become clearer. At 100 km and 200 km depth lower velocities are observed beneath the Afar Depression as well as beneath the Atlas mountains, compared to the initial model. At 300 km and 400 km depth reductions in velocity are seen beneath the East African Rift System. With especially low velocities beneath Lake Victoria in Tanzania.

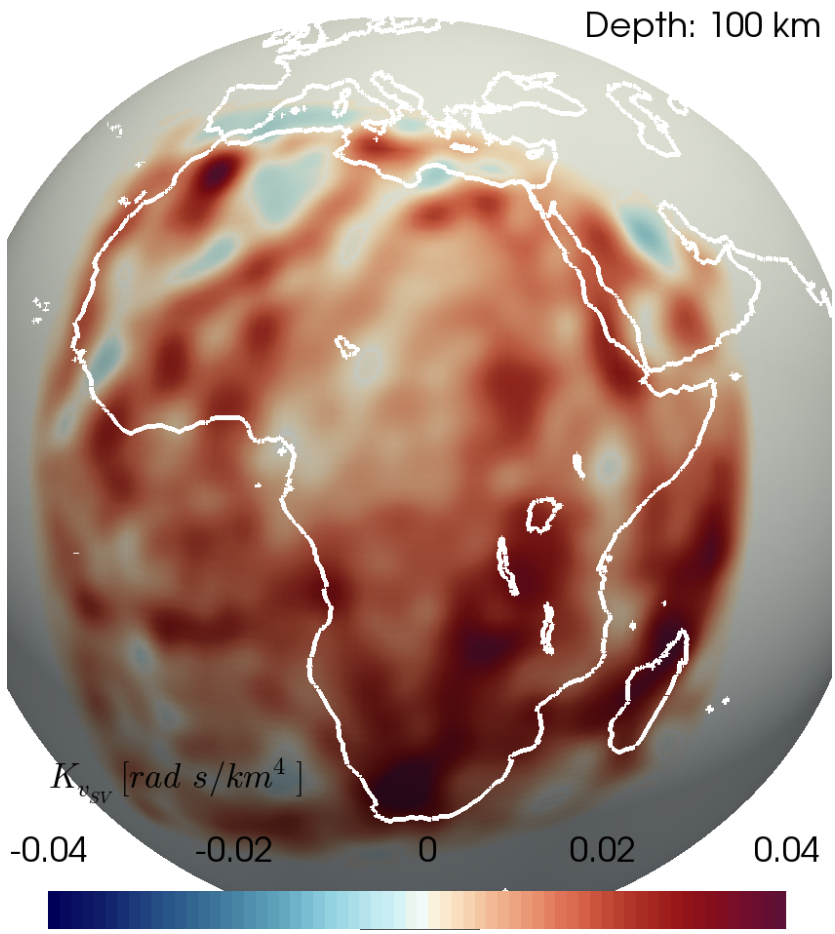

Figure 3-11: Spherical slice of the tapered v_{SV} kernel at iteration 8 at 100 km depth.

This could be part of the African superplume structure as described in Mulibo and Nyblade (2013). In Figure 3-14 and Figure 3-15 v_{SH} initial and final models are shown in a similar fashion as before. The overall trend at 100 km depth is a reduction of v_{SH} compared to the initial model. At the northern edge of the modelled domain the velocity is increasing. This is most likely a result of the paraxial boundary conditions that do not manage to fully absorb the seismic waves. At 200 km, a reduction of v_{SH} beneath the Afar depression can be observed. At 400 km depth increases of velocity can be seen beneath the West African Craton. In Figure 3-16 spherical slices of v_P are shown at 100 and 200 km depth. Here v_P is calculated using the Voigt average. Decreases of P-wave velocity can be seen beneath the Afar region again in the final model compared to the initial model. A more defined structure is observable beneath West African craton. In Figure 3-17 spherical slices at 300 km and 400 km can be seen again. In both new models the low velocity zone beneath the EARS is further decreasing and more clearly defined.

In Figures 3-18, 3-20 and 3-21 the synthetics generated with the initial model (iter_1) and final model (iter_10_weighted) can be observed, along with the preprocessed data. Selected windows are indicated with grey shaded areas. Figure 3-21 shows a convincing case where the match between synthetics and recorded data is improving for the surface waves, even though

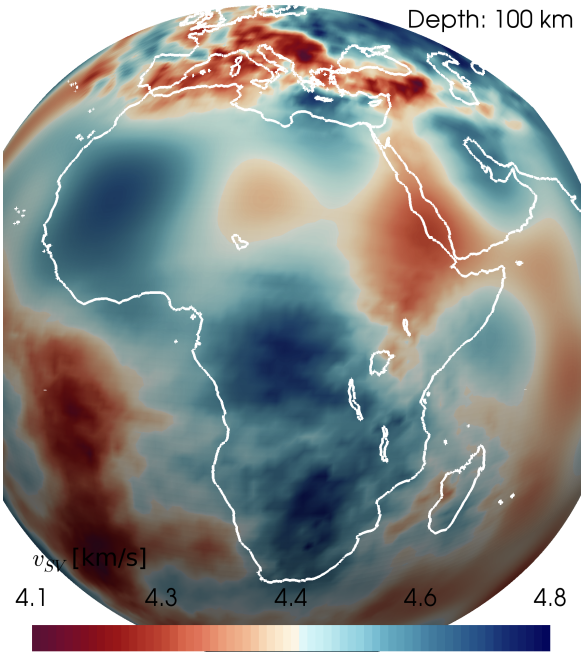

(a) Initial v_{SV} model at 100 km depth.

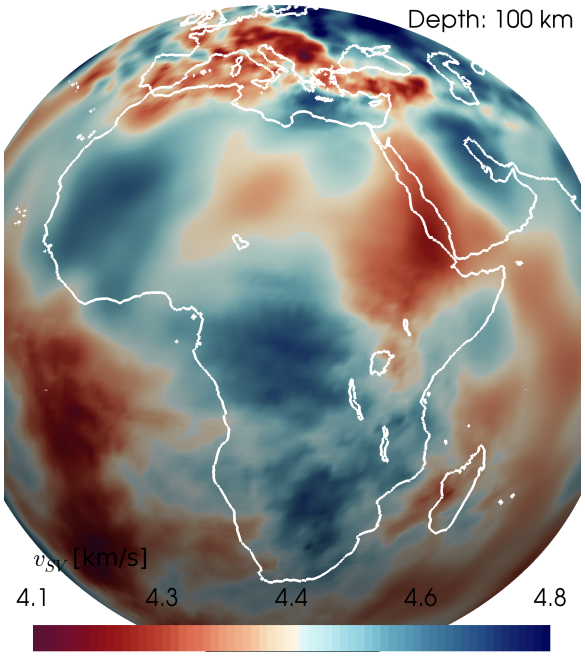

(b) Final v_{SV} model at 100 km depth.

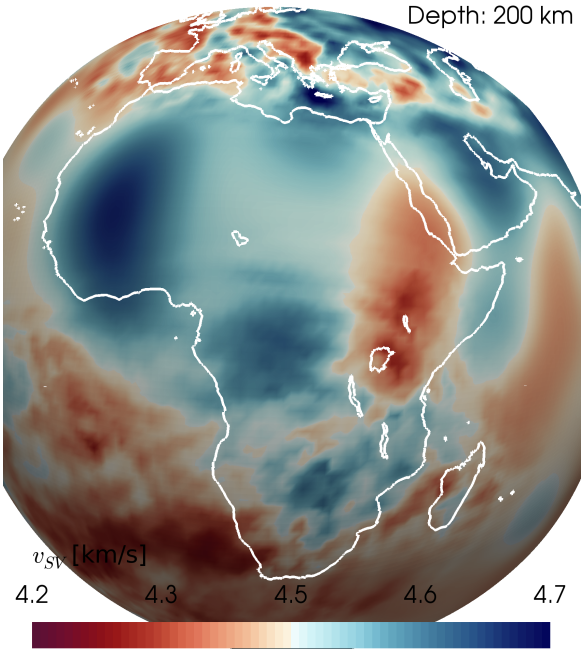

(c) Initial v_{SV} model at 200 km depth.

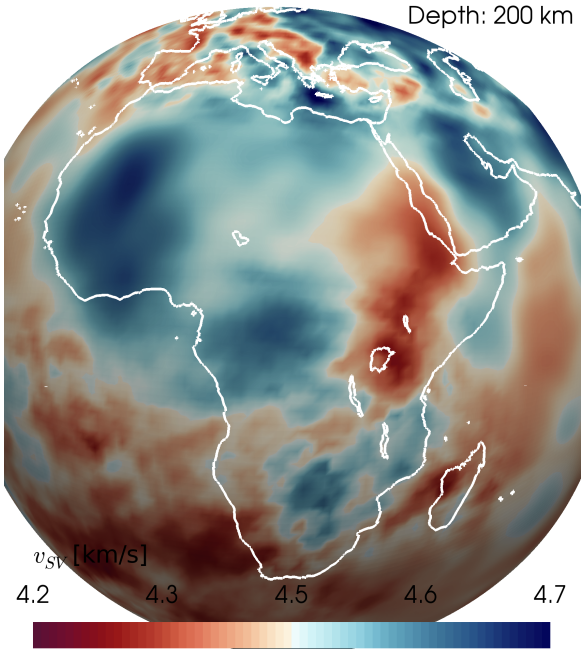

(d) Final v_{SV} model at 200 km depth.

Figure 3-12: Spherical slices of initial (left) and final (right) v_{SV} at 100 km depth (top) and 200 km depth (bottom).

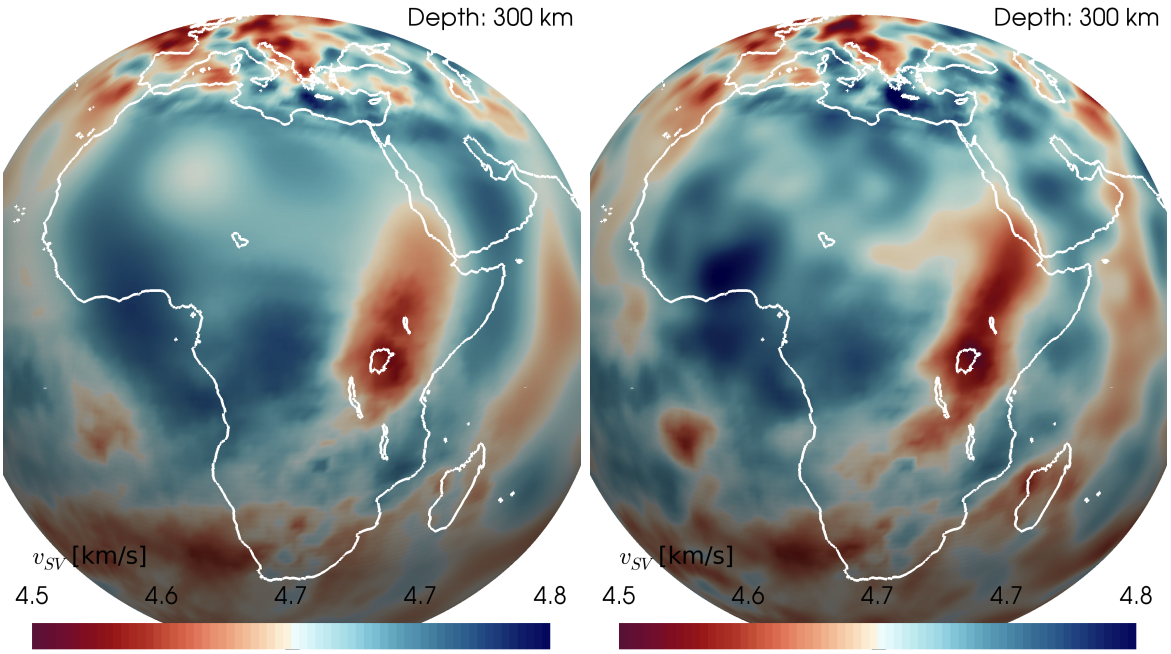

(a) Initial v_{SV} model at 300 km depth.

(b) Final v_{SV} model at 300 km depth.

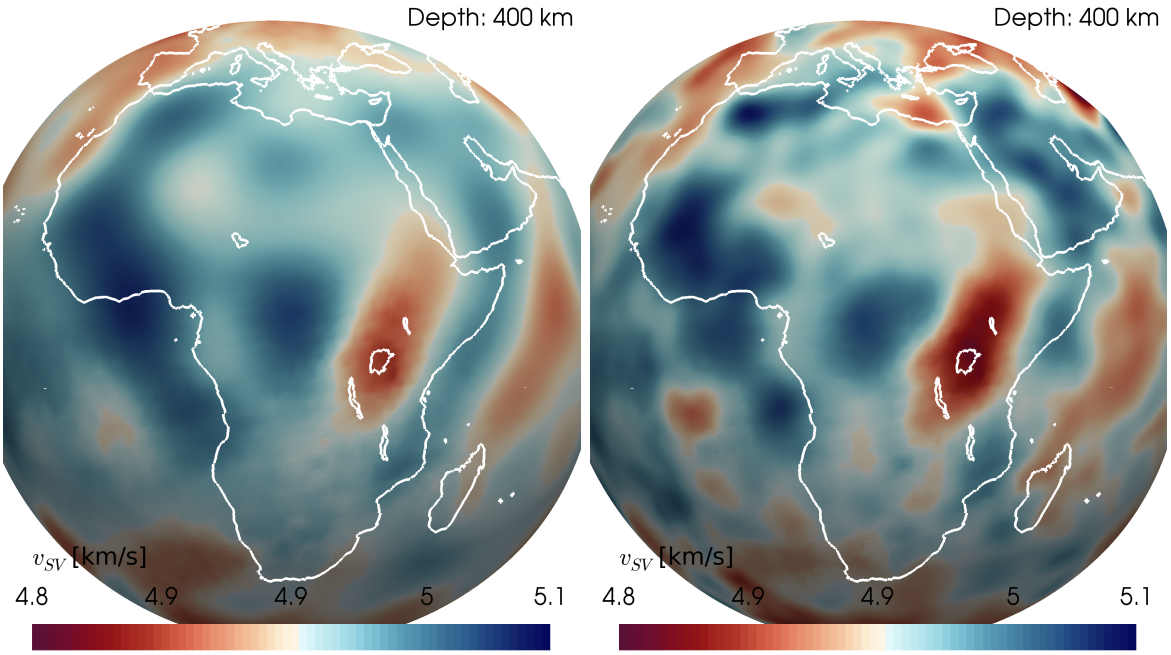

(c) Initial v_{SV} model at 400 km depth.

(d) Final v_{SV} model at 400 km depth.

Figure 3-13: Spherical slices of initial (left) and final (right) v_{SV} at 300 km depth (top) and 400 km depth (bottom).

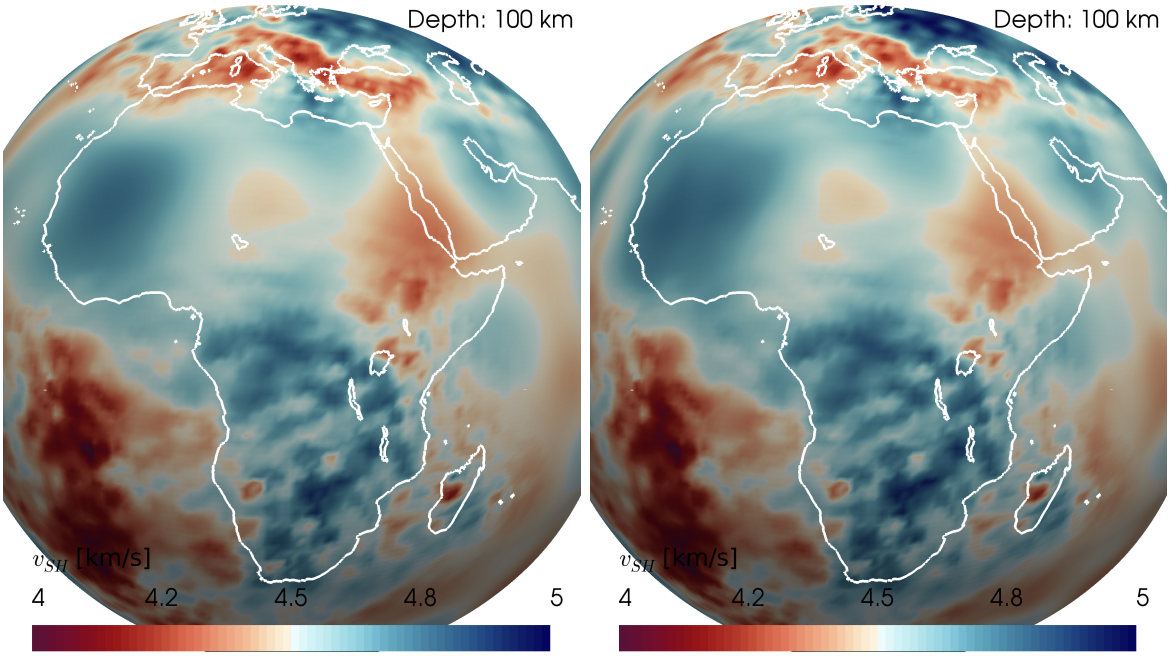

(a) Initial v_{SH} model at 100 km depth.

(b) Final v_{SH} model at 100 km depth.

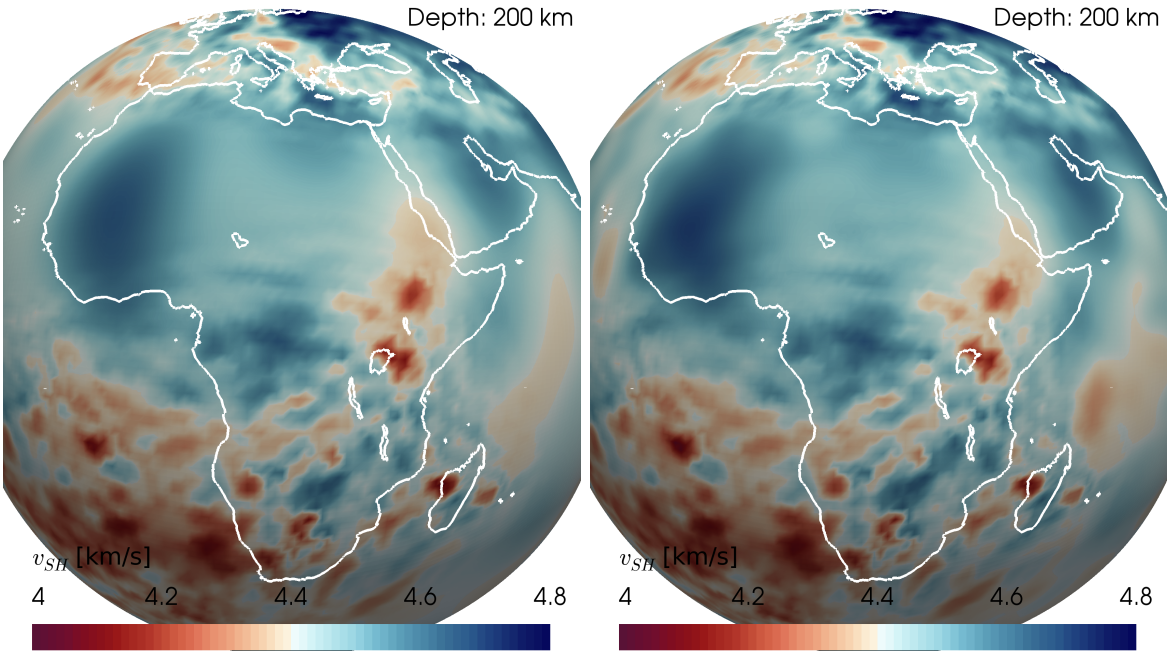

(c) Initial v_{SH} model at 200 km depth.

(d) Final v_{SH} model at 200 km depth.

Figure 3-14: Spherical slices of initial (left) and final (right) v_{SH} at 100 km depth (top) and 200 km depth (bottom).

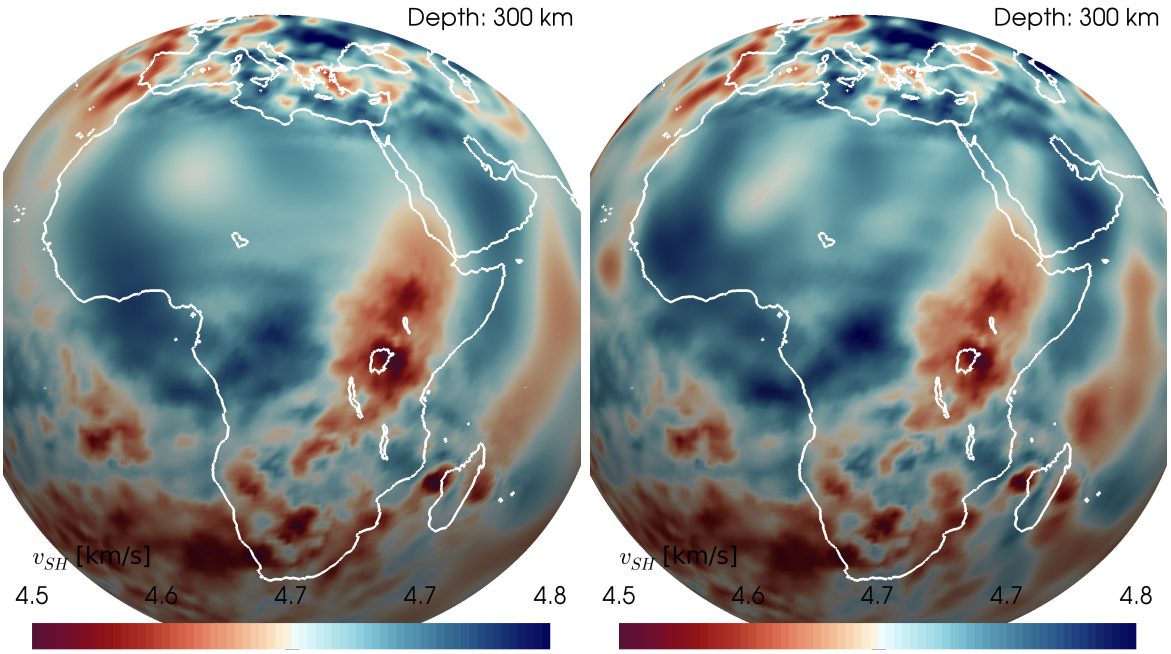

(a) Initial v_{SH} model at 300 km depth.

(b) Final v_{SH} model at 300 km depth.

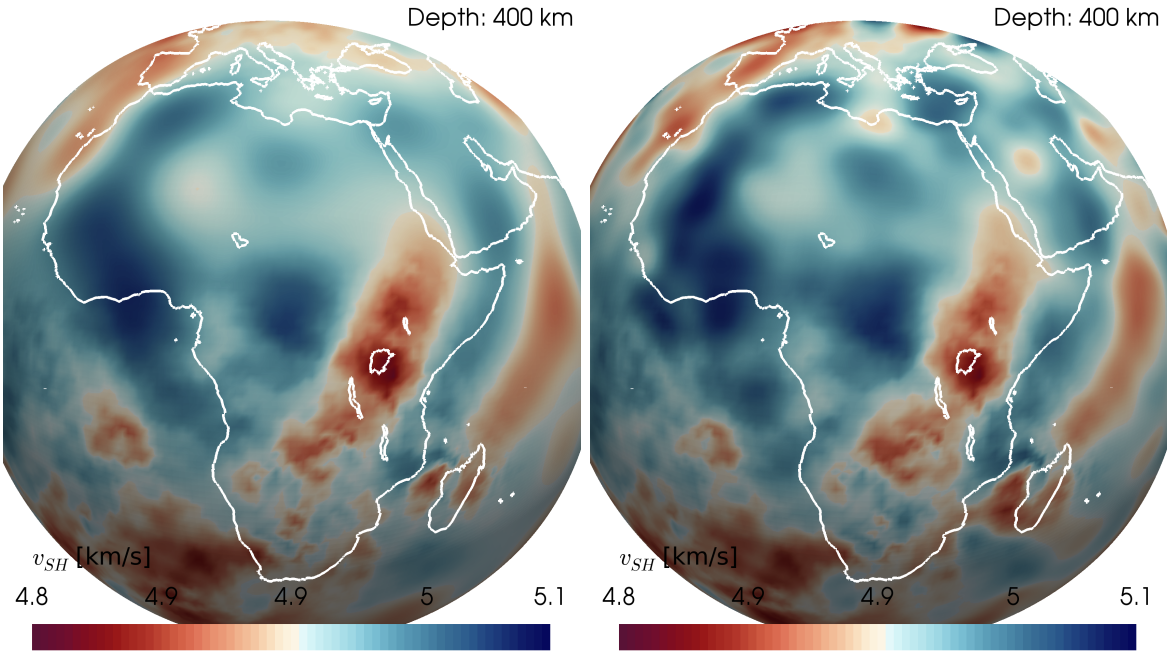

(c) Initial v_{SH} model at 400 km depth.

(d) Final v_{SH} model at 400 km depth.

Figure 3-15: Spherical slices of initial (left) and final (right) v_{SH} at 300 km depth (top) and 400 km depth (bottom).

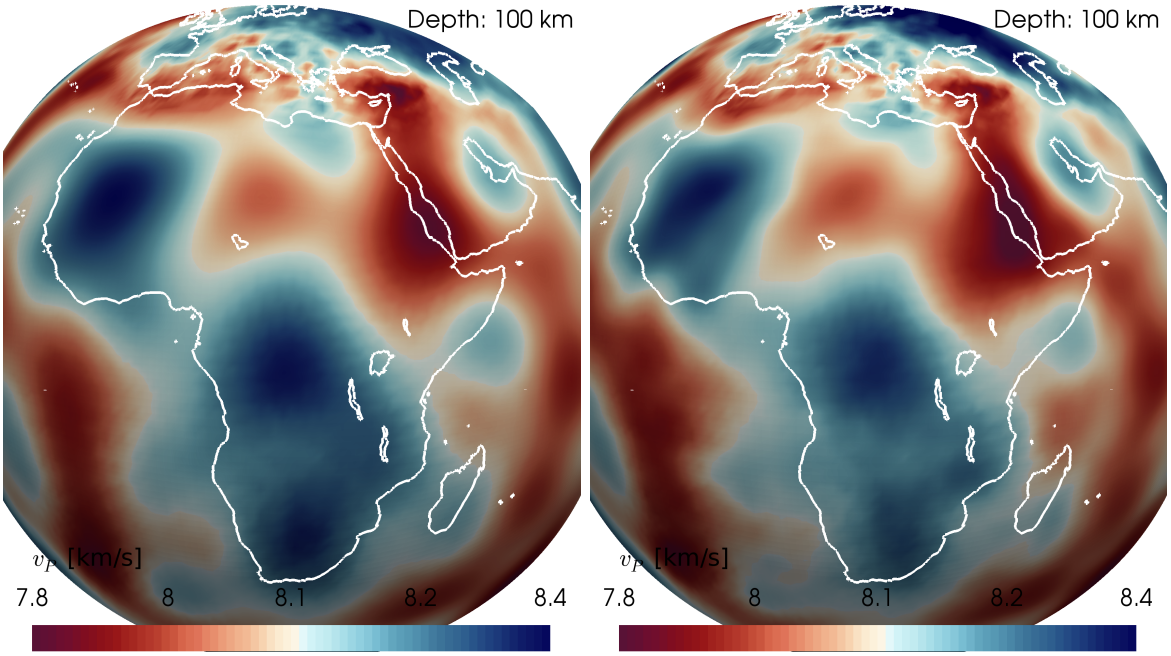

(a) Initial v_P model at 100 km depth.

(b) Final v_P model at 100 km depth.

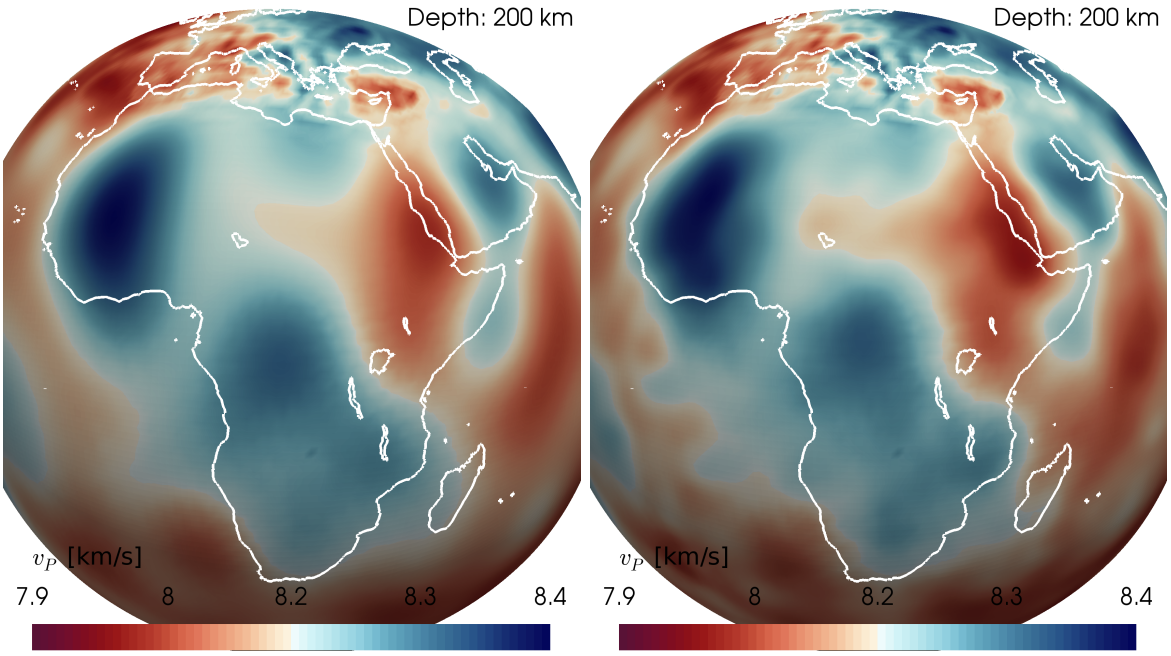

(c) Initial v_P model at 200 km depth.

(d) Final v_P model at 200 km depth.

Figure 3-16: Spherical slices of initial (left) and final (right) v_P at 100 km depth (top) and 200 km depth (bottom).

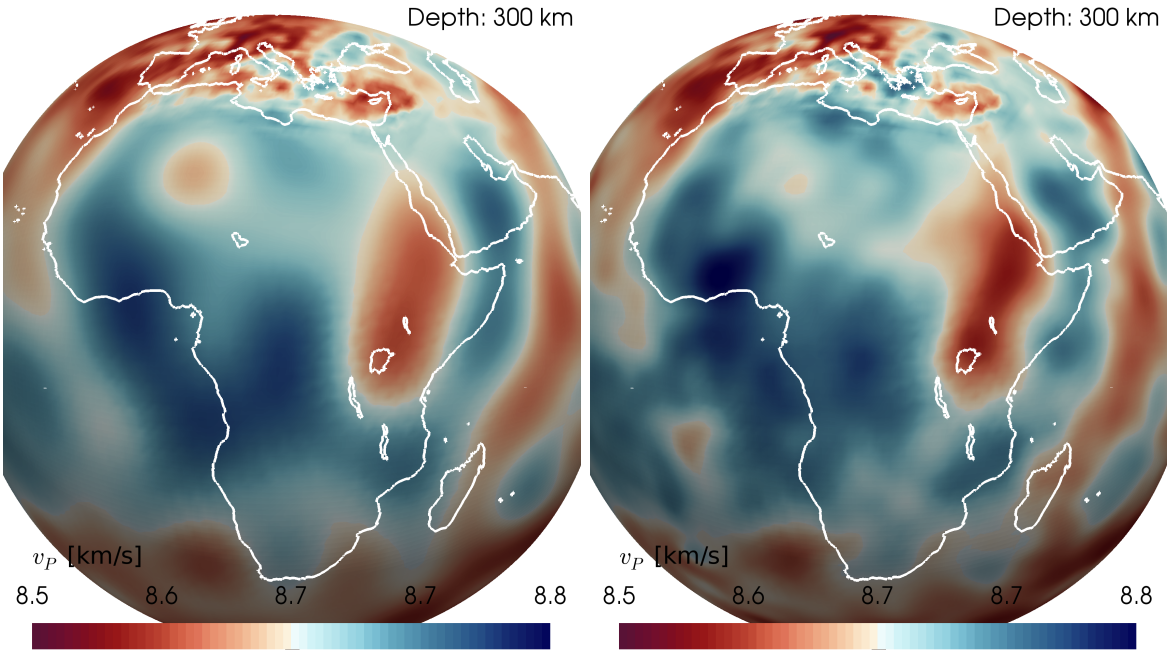

(a) Initial v_P model at 300 km depth.

(b) Final v_P model at 300 km depth.

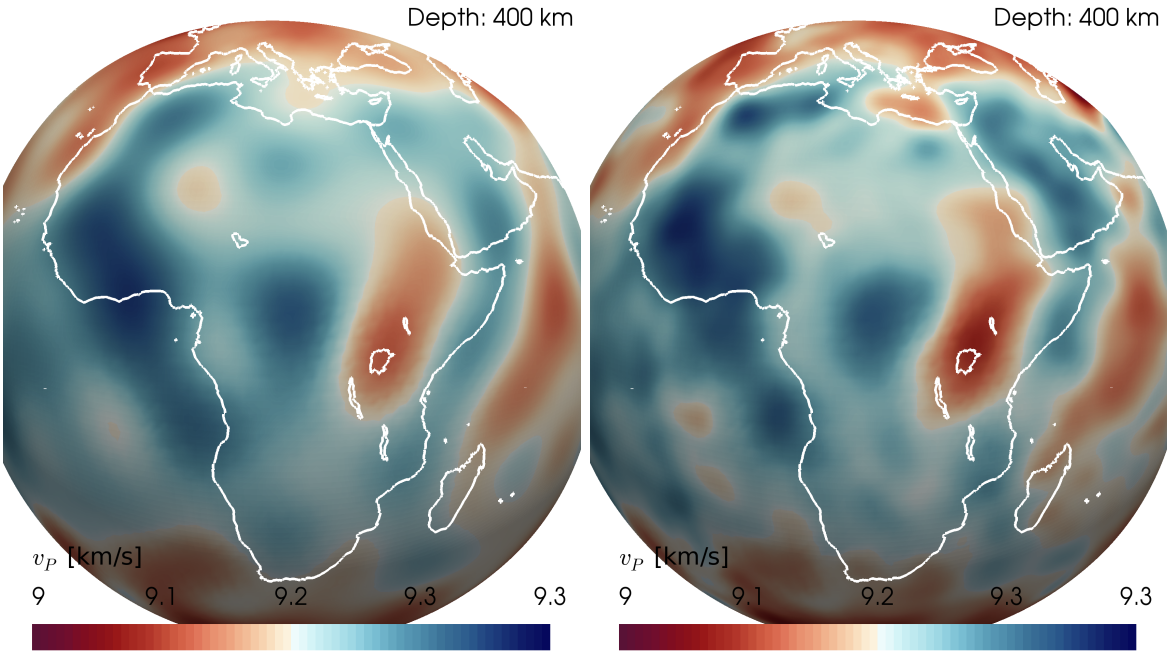

(c) Initial v_P model at 400 km depth.

(d) Final v_P model at 400 km depth.

Figure 3-17: Spherical slices of initial (left) and final (right) v_P at 300 km depth (top) and 400 km depth (bottom).

the window selection algorithm did not not deem the match good enough to be used for the inversion.

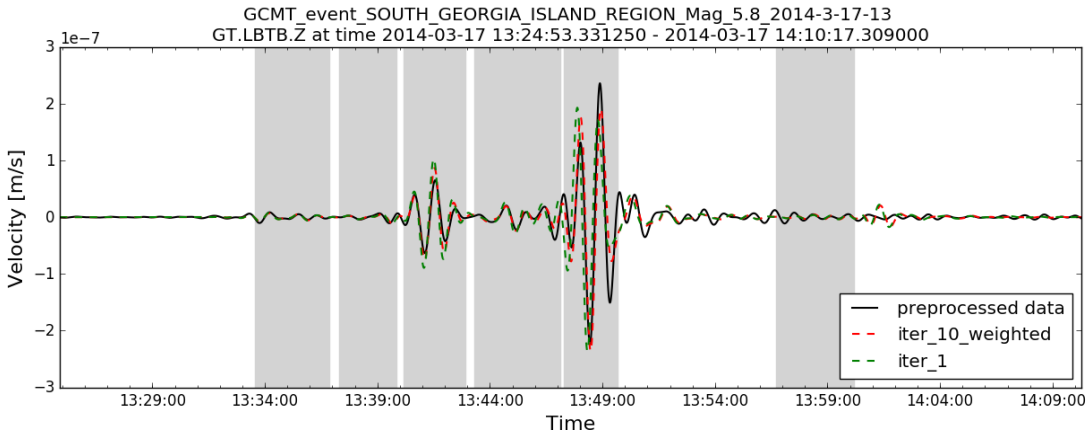

Figure 3-18: An illustration of improvement in data fit.

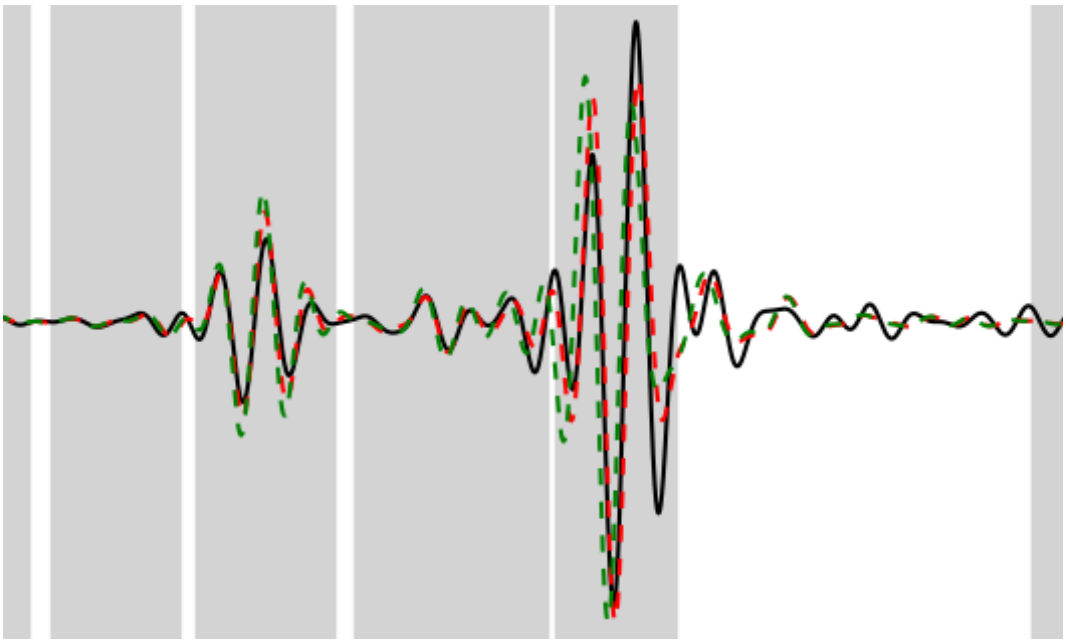

Figure 3-19: A zoom in on Figure 3-18.

3-6-1 Validation

The FWI method is very good at reducing misfits and fitting data. With enough model parameters and without applying too much regularization such as smoothing, the fit will become almost perfect. Even noise can be fit. This does not mean that the found model $\mathbf{m}$ is equal to the optimal model $\widetilde{\mathbf{m}}$. Since the optimal model of the Earth is unknown the only ways to validate the new model are through physical intuition or independent testing with data that was not used for the inversion. To test if the new model also does a better job at

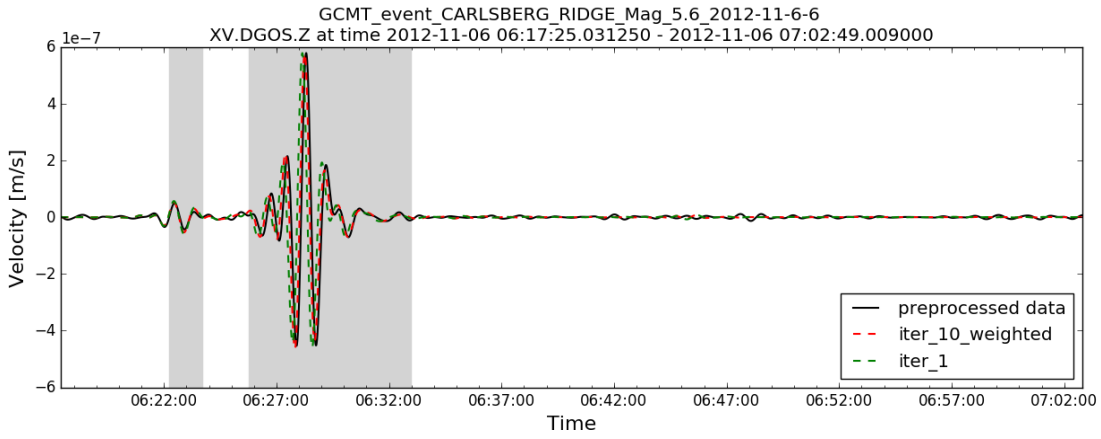

Figure 3-20: An illustration of improvement in data fit.

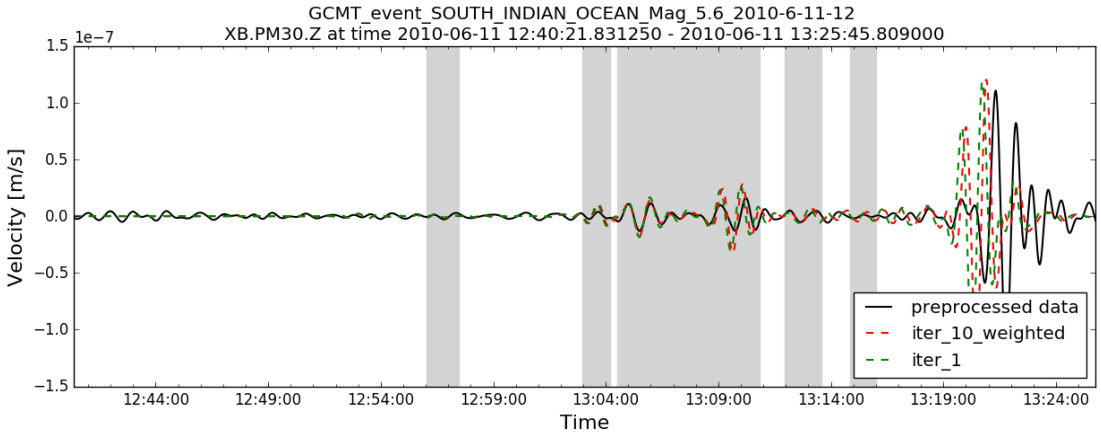

Figure 3-21: An illustration of improvement in data fit. Here the synthetic surface waves can be seen to move closer towards the preprocessed data, even though no window was picked.

explaining other seismic data, a validation test was performed. By using the recordings of ten earthquakes that were not used previously in the inversion, we can evaluate whether we have not over fitted the data. The ray density of the test setup can be seen in Figure 3-22. Two forward simulations were performed, one with the initial model, and one with the final model. Windows were picked for the initial model and misfits were evaluated for both the initial model synthetics and final model synthetics based on time-frequency phase misfits. In table 3-1 the change in misfit for each simulated event is shown. As can be seen the misfits decrease for every tested event. The average decrease in misfit for these events is 7.7 %, with a minimum reduction of 0.77 % and a maximum reduction of 14.27 % in misfit. The decreases in misfit observed during the inversion are of similar magnitudes. This boosts our confidence in the reliability of the model. However because of the likely incorrect updates at the edges of the modelled domain it is safer to discard changes within those regions.

Table 3-1: Earthquakes and relative misfit change, compared to the initial model $\mathbf{m}_0$.

Earthquake event	Change in misfit [%]
PRINCE EDWARD ISLANDS REGION Mag 6.0 2009-6-4-17	-0.77 %
WESTERN GULF OF ADEN Mag 5.6 2009-11-5-7	-1.66 %
SOUTHERN MID-ATLANTIC RIDGE Mag 5.5 2009-6-27-15	-14.27 %
SOUTH SANDWICH ISLANDS REGION Mag 6.7 2009-4-16-14	-7.77 %
CENTRAL MID-ATLANTIC RIDGE Mag 5.6 2009-1-2-19	-13.26 %
HINDU KUSHI REGION AFGHANISTAN Mag 6.1 2009-10-22-19	-11.32 %
MAURITIUS-REUNION REGION Mag 5.8 2009-12-18-7	-13.91 %
MALAWI Mag 6.0 2009-12-19-23	-0.77 %
AZORES ISLANDS REGION Mag 5.9 2009-11-4-18	-11.27 %
IONIAN SEA Mag 5.8 2009-11-3-5	-1.57 %

3-7 Discussion

Throughout the project many choices were made and steps were performed. In almost all of the steps there is most likely room for improvement. To stay in the same chronological order as this thesis we begin with the data. The amount of stations available is limited and has varied over time. To make the most out of the data it could be good to look at the stations that were online for each event and select the best events, based on the optimal coverage of stations. Our approach to simplify this problem was to visualize the station coverage over time and roughly pick the events which had the best coverage. In any case though data is limited and better results are likely, when more data would be recorded. Another option worth exploring to improve data coverage would be to apply source stacking. With source stacking one simulates and inverts for multiple earthquakes simultaneously to reduce the computational cost.

Another improvement on the data side would be to start the inversion only for the very lowest frequencies. We applied a band pass filter that retained the periods between 40 s and 100 s. For some regions this worked perfectly fine and there was proper convergence. However for regions where the initial model was of lesser quality such as beneath Western Africa synthetics and preprocessed, very few windows were selected. With the current knowledge, it may have been better to start converging for the longer periods first.

Another option worth exploring to get more data especially in aseismic areas, is the use of ambient seismic noise cross-correlations. Based on the assumption that the causal part of a noise correlation represents the Green's Function, we modelled the virtual sources as point source in the Z-direction. Going through the same procedure as with the earthquake data, but using cross correlation time shift as a definition of the misfit, we obtained the kernel shown in Figure 3-23. The sparse ray density used for this test can be observed in Figure 3-24. Nonetheless it shows strong similarities to the first kernel obtained from the initial model, as shown in Figure 3-5. This indicates that ambient noise cross-correlations could aid in adding extra sensitivity to kernels obtained from earthquake data. Especially in the large aseismic areas of Africa this could prove useful, when more stations would be placed there.

Continuing with the forward problem. In this study the regional option of SPECFEM3D_GLOBE was used. The choice was made because it allows to simulate the

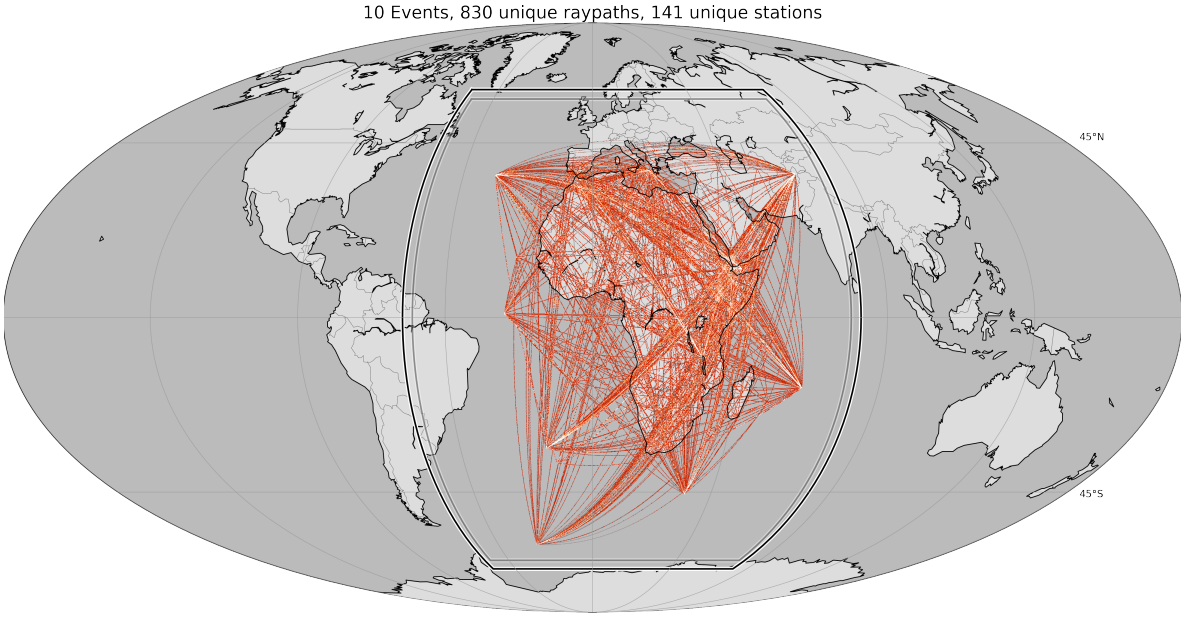

Figure 3-22: Ray coverage of the validation setup.

waves on a chunk of the Earth. This saves computational costs but comes at the cost of having issues with the boundaries and missing seismic phases that travel through the inner core, such as PKP and PKPPKP. The missing phases are only a drawback when they fall within the frequency range of the data used for the inversion, which was not the case for this study. In retrospect, it may have not been worth it to switch to the regional simulation, but it remains a trade off. Saving computational power allows to simulate more earthquakes or perform more iterations. An alternative option could be to increase the angular width of the modelled domain as well as the size of the applied taper depending on the simulation time. This could effectively remove all of the boundary effects while saving computational costs compared to a global simulation.

Also it would make sense to apply the taper from the start and not midway during the iterations. In our case we opted to continue with the disturbed model. In the case of an update to the CSEM model the model perturbations with less certainty such as Europe and the Mediterranean Sea can be discarded, while the perturbations beneath the African continent can be kept.

With respect to the inversion and the model updates, perhaps most improvements could be made by applying different types of smoothing to the kernels. Seismic inverse problems are notorious for their mixed-determinacy. In this study it is clearly visible with the relatively large amounts of stations in Morocco, the Afar region, Tanzania plus surroundings and Madagascar but barely any stations in the rest of Africa e.g. the entire Sahara area. It makes sense to reduce the amount of smoothing in areas with good coverage compared to areas with less coverage, This would likely help to converge quicker and help to reduce the risk of over fitting data in regions where you should be less confident.

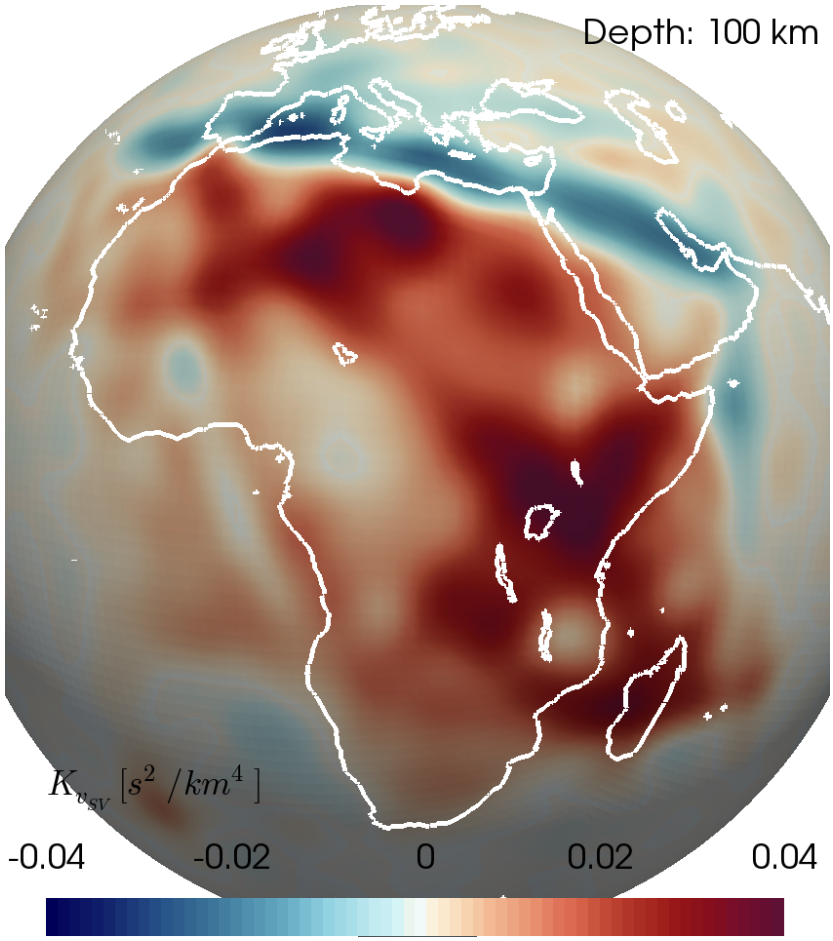

Figure 3-23: Spherical slice of the V_{SV} kernel at 100 km depth, using noise cross-correlations instead of earthquake recordings.

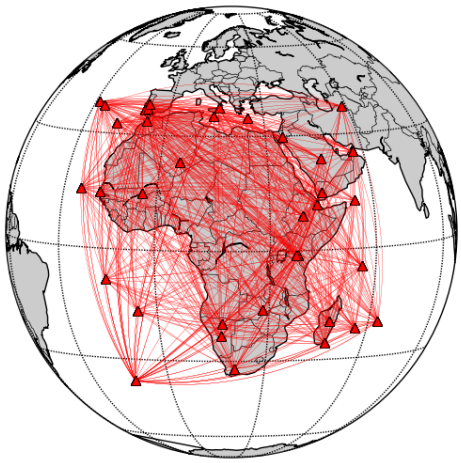

Figure 3-24: Ray coverage of the noise cross-correlations.

3-8 Conclusion

The goal of this project was to improve the seismic model of Africa using the method of Full Waveform Inversion. Obtaining a better model of the Earth has several applications. E.g. to improve understanding of how effects occurring in the mantle are dynamically supporting the African topography, or any other application where a tomographic model from the Earth is required. To our knowledge this been the first attempt to perform a FWI on the entire continent of Africa. In this report a step by step overview was given on the applied methods and a new model was presented, which explains the data better than before.

The 100 earthquakes used were selected from the time period between 2010 and 2015. These years had a relatively good distribution of seismic recording stations. The data was preprocessed and band pass filtered, retaining the waves with periods between 40 s and 100 s. This data served as the input for the inversion procedure.

To drive the inversion the regional simulation option of SPECFEM3D_GLOBE was used. Unfortunately due to boundary conditions at the edges of the domain artefacts were introduced at the edges of the domain. Before this model is implemented back into the CSEM, a critical look has to be taken on which parts can be trusted and which changes to the initial model should be discarded. The small test setup showed a decrease in misfit for all events. However, not the entire modelled domain was covered by the test and it will be safer to discard any updates made within approximately 25 degrees of latitude and longitude from the edges of the domain, where boundary artefacts were strongest. Another option could be to discard the results and start over using the global simulation of SPECFEM3D_GLOBE.

SPECFEM uses the spectral element method to solve the wave field. This method has the main benefit of a diagonal mass matrix, which makes it a trivial operation to invert it. This makes the solver highly efficient. Time-frequency phase misfits were used as a definition of misfit. Using LASIF's window selection algorithm, windows were picked for which adjoint sources were calculated. The adjoint sources and misfits were weighted based on the amount of clustering of the stations. This helped to reduce the sensitivity to regions with a high number of stations and increase the sensitivity for regions with lower amounts of stations, resulting in more balanced model updates and potentially increasing the rate of convergence. With the adjoint sources it was possible to compute kernels with respect to the model parameters for the regions where there was interaction between the regular and adjoint wave fields. The obtained volumetric densities of the gradient to the misfit functional with respect to the model parameters were used to update the model. Steepest descents and conjugate gradient methods were used to minimize the misfit. Step lengths were found with a line search where a parabola was fit through different model perturbations and their corresponding misfits. The process was repeated for several iterations. Additional windows were selected, the kernel was tapered off to remove boundary artefacts and smoothing was reduced. This helped to increase convergence. Ideally the amount of smoothing would depend on the quality of the starting model and the amount of data available. To increase the amount of data available a joint inversion could be performed with both earthquake data and ambient noise cross-correlations. The kernel constructed with the noise data showed similarities and performing a model update with it reduced the misfit.

Spherical slices through final the model show decreases in v_{SV} especially beneath the Afar Depression and the East African Rift System. Outlines of the West African craton have

become more confined. To increase certainty of the new model, ideally more data would be included in future inversions. Earthquakes originating along the Atlantic Ridge do see significant decreases in misfit indicating that the model has improved significantly in areas with the highest ray density. All in all this project has shown that it is feasible to perform a FWI on such a large continent as Africa. With more data, more iterations and likely future increases in computational power, results can only get better.

Bibliography

(2016). IRIS http://www.iris.edu/hq/.

(2016). OvalOffice https://github.com/michael-afanasiev/OvalOffice.

(2016). Piz Daint: CSCS supercomputer http://www.cscs.ch/computers/piz_daint_piz_dora/index.html.

(2016a). SPECFEM3D_GLOBE https://geodynamics.org/cig/software/specfem3d_globe/.

(2016b). SPECFEM3D_GLOBE https://github.com/geodynamics/specfem3d_globe.

Afanasiev, M., Peter, D., Sager, K., Simute, S., Ermert, L., Krischer, L., and Fichtner, A. (2016). Foundations for a multiscale collaborative global Earth model. *Geophysical Journal International*, 204(1):39–58.

Aki, K., Christoffersson, A., and Husebye, E. S. (1977). Determination of the three-dimensional seismic structure of the lithosphere. *Journal of Geophysical Research*, 82(2):277–296.

Aki, K. and Richards, P. G. (2002). *Quantitative seismology*, volume 1.

Bamberger, A., Chavent, G., Hemon, C., and Lailly, P. (1982). Inversion of normal incidence seismograms. *Geophysics*, 47(5):757–770.

Bastow, I., Nyblade, A., Stuart, G., Rooney, T., and Benoit, M. (2008). Upper mantle seismic structure beneath the Ethiopian hot spot: Rifting at the edge of the African low-velocity anomaly. *Geochemistry, Geophysics, Geosystems*, 9(12).

Beyreuther, M., Barsch, R., Krischer, L., Megies, T., Behr, Y., and Wassermann, J. (2010). ObsPy: A Python toolbox for seismology. *Seismological Research Letters*, 81(3):530–533.

Brossier, R., Operto, S., and Virieux, J. (2010). Which data residual norm for robust elastic frequency-domain full waveform inversion? *Geophysics*, 75(3):R37–R46.

Burke, K. (1996). The African plate. *South african journal of geology*, 99(4):341–409.

Cahen, L., Snelling, N., Delhal, J., Vail, J., Bonhomme, M., and Ledent, D. (1984). The Geochronology and Evolution of Africa.

Cande, S. C., Patriat, P., and Dyment, J. (2010). Motion between the Indian, Antarctic and African plates in the early Cenozoic. *Geophysical Journal International*, 183(1):127–149.

Cerveny, V. (2005). *Seismic ray theory*. Cambridge university press.

Colli, L., Fichtner, A., and Bunge, H.-P. (2013). Full waveform tomography of the upper mantle in the South Atlantic region: Imaging a westward fluxing shallow asthenosphere? *Tectonophysics*, 604:26–40.

Doucouré, C. M. and de Wit, M. J. (2003). Old inherited origin for the present near-bimodal topography of Africa. *Journal of African Earth Sciences*, 36(4):371–388.

Duff, P. M. D. and Duff, D. (1993). *Holmes' principles of physical geology*. Taylor & Francis.

Dziewonski, A., Hales, A., and Lapwood, E. (1975). Parametrically simple earth models consistent with geophysical data. *Physics of the Earth and Planetary Interiors*, 10(1):12–48.

Dziewonski, A. M. (1984). Mapping the lower mantle: determination of lateral heterogeneity in P velocity up to degree and order 6. *Journal of Geophysical Research: Solid Earth*, 89(B7):5929–5952.

Dziewonski, A. M. and Anderson, D. L. (1981). Preliminary reference Earth model. *Physics of the earth and planetary interiors*, 25(4):297–356.

Einstein, A. (1916). The foundation of the generalised theory of relativity. *On a Heuristic Point of View about the Creation and Conversion of Light 1 On the Electrodynamics of Moving Bodies 10 The Development of Our Views on the Composition and Essence of Radiation 11 The Field Equations of Gravitation 19 The Foundation of the Generalised Theory of Relativity*, 22:22.

Fichtner, A. (2010). *Full seismic waveform modelling and inversion*. Springer Science & Business Media.

Fichtner, A., Kennett, B. L., Igel, H., and Bunge, H.-P. (2008). Theoretical background for continental-and global-scale full-waveform inversion in the time–frequency domain. *Geophysical Journal International*, 175(2):665–685.

Fichtner, A., Kennett, B. L., Igel, H., and Bunge, H.-P. (2009). Full seismic waveform tomography for upper-mantle structure in the Australasian region using adjoint methods. *Geophysical Journal International*, 179(3):1703–1725.

Fichtner, A., Saygin, E., Taymaz, T., Cupillard, P., Capdeville, Y., and Trampert, J. (2013a). The deep structure of the North Anatolian fault zone. *Earth and Planetary Science Letters*, 373:109–117.

Fichtner, A., Trampert, J., Saygin, E., Cupillard, P., Villasenor, A., Capdeville, Y., and Taymaz, T. (2013b). Multi-scale full waveform inversion for the the crust and upper mantle beneath Europe and western Asia. In *EGU General Assembly Conference Abstracts*, volume 15, page 3465.

Fishwick, S. and Bastow, I. D. (2011). Towards a better understanding of African topography: a review of passive-source seismic studies of the African crust and upper mantle. *Geological Society, London, Special Publications*, 357(1):343–371.

Gee, L. S. and Jordan, T. H. (1992). Generalized seismological data functionals. *Geophysical Journal International*, 111(2):363–390.

Gutenberg, B. (1913). Uber die Konstitution des Erdinnern, erschlossen aus Erdbebenbeobachtungen. *Phys. Z*, 14:1217–1218.

Igel, H., Djikpéssé, H., and Tarantola, A. (1996). Waveform inversion of marine reflection seismograms for P impedance and Poisson's ratio. *Geophysical Journal International*, 124(2):363–371.

Jones, E., Oliphant, T., Peterson, P., et al. (2001). Open source scientific tools for python.

Komatitsch, D., Erlebacher, G., Göddeke, D., and Michéa, D. (2010). High-order finite-element seismic wave propagation modeling with MPI on a large GPU cluster. *Journal of computational physics*, 229(20):7692–7714.

Komatitsch, D. and Tromp, J. (2002a). Spectral-element simulations of global seismic wave propagationI. Validation. *Geophysical Journal International*, 149(2):390–412.

Komatitsch, D. and Tromp, J. (2002b). Spectral-element simulations of global seismic wave propagationII. Three-dimensional models, oceans, rotation and self-gravitation. *Geophysical Journal International*, 150(1):303–318.

Krischer, L., Fichtner, A., Zukauskaite, S., and Igel, H. (2015a). Large-Scale Seismic Inversion Framework. *Seismological Research Letters*.

Krischer, L., Megies, T., Barsch, R., Beyreuther, M., Lecocq, T., Caudron, C., and Wassermann, J. (2015b). ObsPy: A bridge for seismology into the scientific Python ecosystem. *Computational Science & Discovery*, 8(1):014003.

Kristeková, M., Kristek, J., and Moczo, P. (2009). Time-frequency misfit and goodness-of-fit criteria for quantitative comparison of time signals. *Geophysical Journal International*, 178(2):813–825.

Lehmann, I. (1936). P: Publications du Bureau Central Séismologique International. *A14*, pages 87–115.

Makris, J. and Ginzburg, A. (1987). The Afar Depression: transition between continental rifting and sea-floor spreading. *Tectonophysics*, 141(1-3):199–214.

Mallet, R. and Mallet, J. (1858). The earthquake catalogue of the British association. *Brit. Assoc. Adv. Sci. London*.

Meier, U., Curtis, A., and Trampert, J. (2007a). Fully nonlinear inversion of fundamental mode surface waves for a global crustal model. *Geophysical Research Letters*, 34(16).

Meier, U., Curtis, A., and Trampert, J. (2007b). Global crustal thickness from neural network inversion of surface wave data. *Geophysical Journal International*, 169(2):706–722.

Mulibo, G. D. and Nyblade, A. A. (2013). Mantle transition zone thinning beneath eastern Africa: Evidence for a whole-mantle superplume structure. *Geophysical Research Letters*, 40(14):3562–3566.

Oldham, R. (1906). The constitution of the earth. *Quarterly Journal of the Geological Society of London*, 62:456–475.

Pasyanos, M. E. and Nyblade, A. A. (2007). A top to bottom lithospheric study of Africa and Arabia. *Tectonophysics*, 444(1):27–44.

Patera, A. T. (1984). A spectral element method for fluid dynamics: laminar flow in a channel expansion. *Journal of computational Physics*, 54(3):468–488.

Pratt, R. G. (1999). Seismic waveform inversion in the frequency domain, Part 1: Theory and verification in a physical scale model. *Geophysics*, 64(3):888–901.

Pratt, R. G., Shin, C., and Hick, G. (1998). Gauss–Newton and full Newton methods in frequency–space seismic waveform inversion. *Geophysical Journal International*, 133(2):341–362.

Ritsema, J. and van Heijst, H. (2000). New seismic model of the upper mantle beneath Africa. *Geology*, 28(1):63–66.

Ritsema, J., van Heijst, H. J., and Woodhouse, J. H. (1999). Complex shear wave velocity structure imaged beneath Africa and Iceland. *Science*, 286(5446):1925–1928.

Spetzler, J., Trampert, J., and Snieder, R. (2001). Are we exceeding the limits of the great circle approximation in global surface wave tomography? *Geophysical research letters*, 28(12):2341–2344.

Tarantola, A. (1984). Linearized inversion of seismic reflection data. *Geophysical prospecting*, 32(6):998–1015.

Tarantola, A. (1986). A strategy for nonlinear elastic inversion of seismic reflection data. *Geophysics*, 51(10):1893–1903.

Teixell, A., Ayarza, P., Zeyen, H., Fernandez, M., and Arboleya, M.-L. (2005). Effects of mantle upwelling in a compressional setting: the Atlas Mountains of Morocco. *Terra Nova*, 17(5):456–461.

Torsvik, T. H., Müller, R. D., Van der Voo, R., Steinberger, B., and Gaina, C. (2008). Global plate motion frames: toward a unified model. *Reviews of Geophysics*, 46(3).

Torsvik, T. H., Rousse, S., Labails, C., and Smethurst, M. A. (2009). A new scheme for the opening of the South Atlantic Ocean and the dissection of an Aptian salt basin. *Geophysical Journal International*, 177(3):1315–1333.

Tromp, J., Tape, C., and Liu, Q. (2005). Seismic tomography, adjoint methods, time reversal and banana-doughnut kernels. *Geophysical Journal International*, 160(1):195–216.

Tsvankin, I. (2012). *Seismic signatures and analysis of reflection data in anisotropic media*. Number 19. SEG Books.

Williamson, P. (1991). A guide to the limits of resolution imposed by scattering in ray tomography. *Geophysics*, 56(2):202–207.

Zhou, C., Cai, W., Luo, Y., Schuster, G. T., and Hassanzadeh, S. (1995). Acoustic wave-equation traveltime and waveform inversion of crosshole seismic data. *Geophysics*, 60(3):765–773.

Appendix A

Used Data

A-1 Events

Index	Events
0	GCMT event AEGEAN SEA Mag 5.8 2013-1-8-14
1	GCMT event AFGHANISTAN-TAJIKISTAN BORD REG. Mag 5.7 2012-5-12-23
2	GCMT event AFGHANISTAN-TAJIKISTAN BORD REG. Mag 5.7 2012-7-19-7
3	GCMT event ARMENIA-AZERBAIJAN-IRAN BORD REG Mag 6.5 2012-8-11-12
4	GCMT event ASCENSION ISLAND REGION Mag 6.0 2011-8-10-23
5	GCMT event AZORES ISLANDS REGION Mag 5.8 2013-4-30-6
6	GCMT event BOUVET ISLAND REGION Mag 5.8 2013-4-20-5
7	GCMT event BULGARIA Mag 5.6 2012-5-22-0
8	GCMT event CARLSBERG RIDGE Mag 5.5 2012-3-17-17
9	GCMT event CARLSBERG RIDGE Mag 5.5 2013-9-24-7
10	GCMT event CARLSBERG RIDGE Mag 5.5 2014-9-30-16
11	GCMT event CARLSBERG RIDGE Mag 5.6 2012-11-6-6
12	GCMT event CARLSBERG RIDGE Mag 5.6 2012-4-24-9
13	GCMT event CARLSBERG RIDGE Mag 5.6 2013-11-8-9
14	GCMT event CENTRAL MID-ATLANTIC RIDGE Mag 5.5 2012-8-16-12
15	GCMT event CENTRAL MID-ATLANTIC RIDGE Mag 5.6 2010-8-2-3
16	GCMT event CENTRAL MID-ATLANTIC RIDGE Mag 5.6 2011-7-8-5
17	GCMT event CENTRAL MID-ATLANTIC RIDGE Mag 5.6 2013-2-18-3
18	GCMT event CENTRAL MID-ATLANTIC RIDGE Mag 5.9 2014-3-29-7
19	GCMT event CRETE GREECE Mag 6.1 2011-4-1-13
20	GCMT event CRETE GREECE Mag 6.1 2013-6-16-21
21	GCMT event EASTERN CAUCASUS Mag 5.9 2012-5-7-4
22	GCMT event EASTERN MEDITERRANEAN SEA Mag 5.7 2012-7-9-13
23	GCMT event EASTERN MEDITERRANEAN SEA Mag 5.9 2013-12-28-15
24	GCMT event EAST OF SOUTH SANDWICH ISLANDS Mag 5.8 2014-7-26-11

25	GCMT event EAST OF SOUTH SANDWICH ISLANDS Mag 6.2 2012-4-17-19
26	GCMT event EAST OF SOUTH SANDWICH ISLANDS Mag 6.6 2013-10-24-19
27	GCMT event ETHIOPIA Mag 5.6 2011-6-17-9
28	GCMT event GREECE Mag 6.0 2014-2-3-3
29	GCMT event HINDU KUSH REGION AFGHANISTAN Mag 5.6 2010-4-18-20
30	GCMT event HINDU KUSH REGION AFGHANISTAN Mag 5.7 2012-6-11-5
31	GCMT event IRAN-IRAQ BORDER REGION Mag 5.6 2014-8-20-10
32	GCMT event IRAN-IRAQ BORDER REGION Mag 5.7 2013-11-22-6
33	GCMT event MAURITIUS - REUNION REGION Mag 6.3 2010-8-16-3
34	GCMT event MID-INDIAN RIDGE Mag 5.6 2014-8-2-10
35	GCMT event MID-INDIAN RIDGE Mag 5.7 2010-9-3-4
36	GCMT event NORTHERN ALGERIA Mag 5.6 2014-8-1-4
37	GCMT event NORTHERN AND CENTRAL IRAN Mag 5.8 2010-8-27-19
38	GCMT event NORTHERN AND CENTRAL IRAN Mag 5.8 2012-12-5-17
39	GCMT event NORTHERN MID-ATLANTIC RIDGE Mag 5.5 2014-8-30-15
40	GCMT event NORTHERN MID-ATLANTIC RIDGE Mag 5.6 2014-7-4-21
41	GCMT event NORTHERN MID-ATLANTIC RIDGE Mag 5.7 2011-11-18-6
42	GCMT event NORTHERN MID-ATLANTIC RIDGE Mag 5.8 2010-2-27-19
43	GCMT event NORTHERN MID-ATLANTIC RIDGE Mag 6.0 2013-9-5-4
44	GCMT event NORTHERN MID-ATLANTIC RIDGE Mag 6.1 2014-7-27-1
45	GCMT event NORTHWESTERN CAUCASUS Mag 5.8 2012-12-23-13
46	GCMT event NORTH OF ASCENSION ISLAND Mag 5.6 2012-5-9-14
47	GCMT event NORTH OF ASCENSION ISLAND Mag 5.7 2014-6-30-1
48	GCMT event NORTH OF ASCENSION ISLAND Mag 5.9 2013-12-28-18
49	GCMT event OWEN FRACTURE ZONE REGION Mag 5.5 2012-2-4-21
50	GCMT event OWEN FRACTURE ZONE REGION Mag 5.8 2013-10-2-1
51	GCMT event OWEN FRACTURE ZONE REGION Mag 5.9 2013-5-27-3
52	GCMT event PAKISTAN Mag 5.6 2014-9-25-2
53	GCMT event PRINCE EDWARD ISLANDS REGION Mag 5.6 2013-9-6-2
54	GCMT event PRINCE EDWARD ISLANDS REGION Mag 6.3 2013-7-22-7
55	GCMT event RED SEA Mag 5.5 2013-7-8-15
56	GCMT event SCOTIA SEA Mag 5.5 2013-11-16-9
57	GCMT event SOUTHEASTERN AFGHANISTAN Mag 5.5 2013-4-24-9
58	GCMT event SOUTHEASTERN UZBEKISTAN Mag 5.8 2013-5-26-6
59	GCMT event SOUTHERN GREECE Mag 5.6 2014-4-4-20
60	GCMT event SOUTHERN GREECE Mag 5.8 2012-4-16-11
61	GCMT event SOUTHERN IRAN Mag 5.5 2013-5-18-10
62	GCMT event SOUTHERN IRAN Mag 5.7 2013-4-17-3
63	GCMT event SOUTHERN IRAN Mag 5.8 2010-7-20-19
64	GCMT event SOUTHERN IRAN Mag 6.3 2013-4-9-11
65	GCMT event SOUTHERN IRAN Mag 6.5 2010-12-20-18
66	GCMT event SOUTHERN MID-ATLANTIC RIDGE Mag 5.5 2010-1-6-16
67	GCMT event SOUTHERN MID-ATLANTIC RIDGE Mag 5.6 2010-2-26-0
68	GCMT event SOUTHERN MID-ATLANTIC RIDGE Mag 5.6 2014-4-1-23

69	GCMT event SOUTHERN MID-ATLANTIC RIDGE Mag 5.7 2011-4-24-21
70	GCMT event SOUTHERN MID-ATLANTIC RIDGE Mag 5.7 2013-5-16-5
71	GCMT event SOUTHERN MID-ATLANTIC RIDGE Mag 5.7 2013-6-7-20
72	GCMT event SOUTHERN MID-ATLANTIC RIDGE Mag 5.8 2010-1-27-17
73	GCMT event SOUTHERN MID-ATLANTIC RIDGE Mag 5.8 2013-5-10-19
74	GCMT event SOUTHERN MID-ATLANTIC RIDGE Mag 5.8 2014-6-13-19
75	GCMT event SOUTHERN MID-ATLANTIC RIDGE Mag 5.9 2011-3-22-13
76	GCMT event SOUTHWEST INDIAN RIDGE Mag 5.6 2012-3-26-16
77	GCMT event SOUTHWEST INDIAN RIDGE Mag 5.8 2013-4-2-14
78	GCMT event SOUTHWEST INDIAN RIDGE Mag 5.8 2013-8-25-16
79	GCMT event SOUTHWEST INDIAN RIDGE Mag 6.2 2013-8-17-16
80	GCMT event SOUTH ATLANTIC OCEAN Mag 5.8 2012-6-29-15
81	GCMT event SOUTH GEORGIA ISLAND REGION Mag 5.8 2014-3-17-13
82	GCMT event SOUTH INDIAN OCEAN Mag 5.6 2010-6-11-12
83	GCMT event SOUTH OF AFRICA Mag 5.6 2013-12-2-12
84	GCMT event SOUTH OF AFRICA Mag 5.6 2013-5-18-4
85	GCMT event SOUTH OF AFRICA Mag 5.9 2011-12-23-19
86	GCMT event SOUTH SANDWICH ISLANDS REGION Mag 5.5 2010-9-4-11
87	GCMT event SOUTH SANDWICH ISLANDS REGION Mag 5.5 2012-1-13-16
88	GCMT event SOUTH SANDWICH ISLANDS REGION Mag 5.6 2010-3-11-6
89	GCMT event SOUTH SANDWICH ISLANDS REGION Mag 5.6 2014-8-24-20
90	GCMT event SOUTH SANDWICH ISLANDS REGION Mag 5.7 2014-5-19-22
91	GCMT event SOUTH SANDWICH ISLANDS REGION Mag 6.0 2011-7-15-13
92	GCMT event SPAIN Mag 6.3 2010-4-11-22
93	GCMT event TAJIKISTAN Mag 6.2 2011-7-19-19
94	GCMT event TRISTAN DA CUNHA REGION Mag 5.5 2012-9-14-7
95	GCMT event TURKEY Mag 5.5 2010-3-8-7
96	GCMT event TURKEY Mag 5.6 2011-9-22-3
97	GCMT event TURKEY Mag 5.7 2011-11-9-19
98	GCMT event TURKEY Mag 5.9 2011-5-19-20
99	GCMT event UGANDA Mag 5.7 2013-7-3-19

A-2 Stations

Index	Station	Latitude	Longitude
0	AC.KBN	40.6236	20.787399
1	AC.PHP	41.6847	20.4408
2	AC.SRN	39.880001	20.0005
3	AC.VLO	40.468601	19.495501
4	AF.AAUS	9.0349	38.7665
5	AF.ANKE	9.5827	39.7418
6	AF.BLWY	-20.143	28.6113
7	AF.BLWY	-20.143	28.611

8	AF.BOBN	-1.66	29.23666
9	AF.CVNA	-31.482	19.762
10	AF.DESE	11.118	39.635
11	AF.DODT	-6.186	35.748
12	AF.EKNA	4.234	9.328
13	AF.GETA	-2.866	33.241
14	AF.GRM	-33.313	26.508
15	AF.HVD	-30.605	25.497
16	AF.IFE	7.546667	4.45692
17	AF.KTWE	-12.814	28.209
18	AF.KUKU	6.19232	-0.36842
19	AF.LBB	-11.631	27.485
20	AF.MBEY	-9.0	33.25
21	AF.MONG	-15.15	23.09
22	AF.MOPA	-23.517	31.398
23	AF.MTVE	-10.25	40.167
24	AF.MZM	-11.434	34.035
25	AF.NBI	-1.2739	36.8037
26	AF.PKA	-29.67	22.757
27	AF.POGA	-27.346	31.707
28	AF.PWET	-8.28	28.53
29	AF.SEK	-28.323	27.625
30	AF.SHAI	5.88136	0.04389
31	AF.SKRH	-22.827	44.733
32	AF.SVMA	16.84039	-24.925
33	AF.SWZ	-27.182	25.332
34	AF.TEBE	0.0536	32.483
35	AF.TEZI	-15.747	26.016
36	AF.UPI	-28.362	21.253
37	AF.WIN	-22.5667	17.1
38	AF.YNDE	3.87	11.456
39	AF.ZOMB	-15.3833	35.35
40	G.ATD	11.530725	42.846634
41	G.FOMA	-24.97565	46.978877
42	G.MBO	14.392024	-16.955467
43	G.RER	-21.1712	55.73986
44	G.TAM	22.79149	5.52838
45	G.TRIS	-37.0681	-12.3152
46	GE.DAMY	14.5725	44.391701
47	GE.EIL	29.669901	34.951199
48	GE.SOCY	12.18703	53.987419
49	GT.BOSA	-28.6141	25.25553
50	GT.DBIC	6.67016	-4.85656
51	GT.DBIC	6.67015	-4.85653

52	GT.LBTB	-25.0151	25.59665
53	HL.ITM	37.17872	21.92522
54	HL.RDO	41.14503	25.53553
55	II.ABKT	37.9304	58.1189
56	II.ABPO	-19.018	47.229
57	II.ASCN	-7.9327	-14.3601
58	II.MBAR	-0.6019	30.7382
59	II.MSEY	-4.6737	55.4792
60	II.RAYN	23.5225	45.5032
61	II.SACV	14.9702	-23.6085
62	II.SHEL	-15.9588	-5.7457
63	II.SUR	-32.3797	20.8117
64	II.UOSS	24.9453	56.2042
65	IP.MTOR	28.4948	-9.8487
66	IU.ANTO	39.868	32.7934
67	IU.FURI	8.8952	38.6798
68	IU.GNI	40.148	44.741
69	IU.KMBO	-1.1271	37.2525
70	IU.KOWA	14.4967	-4.014
71	IU.LSZ	-15.2779	28.1882
72	IU.MACI	28.2502	-16.508199
73	IU.MSKU	-1.6557	13.6116
74	IU.PAB	39.5446	-4.3499
75	IU.TRIS	-37.0681	-12.3152
76	IU.TSUM	-19.2022	17.5838
77	KO.BALB	39.64	27.88
78	KO.BNN	38.8522	35.8472
79	KO.BZK	41.96	34.0035
80	KO.DKL	39.0713	26.9053
81	KO.ELL	36.7483	29.9085
82	KO.GAZ	37.1722	37.2097
83	KO.GURO	38.5509	42.03222
84	KO.KARS	40.6152	43.0937
85	KO.MDUB	40.4712	31.1977
86	KO.SIRT	37.501	42.4392
87	KW.MIB	29.8032	47.3388
88	LX.GGNV	38.7185	-9.1505
89	LX.MESJ	37.83954	-8.21994
90	LX.MORF	37.304323	-8.652672
91	MN.CEL	38.2603	15.8939
92	MN.CLTB	37.578	13.216
93	MN.CUC	39.9938	15.8155
94	MN.IDI	35.288	24.89
95	MN.RTC	33.9881	-6.8569

96	MN.TIP	39.1794	16.7583
97	MN.TIR	41.3472	19.8631
98	MN.VSL	39.496	9.378
99	MN.WDD	35.8373	14.5242
100	NJ.AWK	6.243	7.112
101	NJ.IFE	7.55	4.547
102	NJ.KAD	10.435	7.6414
103	NJ.NSU	6.867	7.417
104	NJ.TORO	10.986	8.118
105	PM.PESTR	38.867199	-7.590199
106	PM.PFVI	37.132832	-8.826829
107	PM.PMOZ	32.823002	-17.19717
108	PM.PVAQ	37.4037	-7.7173
109	SS.COI	40.20799	-8.4124
110	TT.TATN	32.5787	10.5292
111	XB.PM01	35.7016	-5.6543
112	XB.PM02	35.6101	-5.3471
113	XB.PM03	35.5104	-5.7713
114	XB.PM04	35.4026	-5.1525
115	XB.PM05	35.2134	-5.3368
116	XB.PM06	35.3086	-5.639
117	XB.PM07	35.2275	-4.9863
118	XB.PM08	35.1448	-4.7082
119	XB.PM09	35.0273	-5.1145
120	XB.PM10	34.7379	-5.1368
121	XB.PM11	34.9308	-4.3119
122	XB.PM12	34.8505	-4.6084
123	XB.PM13	34.6723	-4.9354
124	XB.PM14	34.5522	-5.1267
125	XB.PM15	34.4694	-4.6997
126	XB.PM16	35.1304	-3.6948
127	XB.PM17	34.3914	-5.2954
128	XB.PM18	34.15	-4.8195
129	XB.PM19	34.1427	-5.1308
130	XB.PM20	33.9064	-5.0329
131	XB.PM21	33.7205	-5.3197
132	XB.PM22	33.2947	-5.1071
133	XB.PM22B	33.3079	-5.1024
134	XB.PM23	33.128	-5.03
135	XB.PM24	32.9953	-4.8979
136	XB.PM25	32.8757	-4.888
137	XB.PM26	32.5245	-4.5659
138	XB.PM27	32.3499	-4.6537
139	XB.PM28	32.2317	-4.6171

140	XB.PM29	32.0844	-4.3913
141	XB.PM30	31.8634	-4.2718
142	XB.PM30A	31.823	-4.2715
143	XB.PM31	32.7063	-4.7195
144	XB.PM31A	32.7186	-4.739
145	XB.PM32	31.568	-4.1914
146	XB.PM33	31.4318	-4.2427
147	XB.PM33A	31.414	-4.2897
148	XB.PM34	31.2912	-4.1068
149	XB.PM35	31.0463	-3.9958
150	XB.PM36	34.8894	-3.7359
151	XB.PM37	34.9507	-3.1506
152	XB.PM38	34.8385	-2.8737
153	XB.PM39	34.889	-2.6104
154	XB.PM40	34.9075	-2.2104
155	XB.PS01	36.08	-5.6236
156	XB.PS02	36.2564	-5.3708
157	XB.PS03	36.3932	-5.415
158	XB.PS04	36.6051	-5.3228
159	XB.PS05	36.6457	-5.0938
160	XB.PS06	36.7314	-5.5144
161	XB.PS07	36.6706	-4.7988
162	XB.PS08	36.741	-4.643
163	XB.PS09	36.8235	-5.2325
164	XB.PS10	36.8025	-4.9044
165	XB.PS11	36.8728	-4.6805
166	XB.PS12	37.0506	-5.1867
167	XB.PS13	37.0573	-4.7495
168	XB.PS14	37.1475	-5.5178
169	XB.PS15	37.1409	-4.5028
170	XB.PS16	37.2131	-5.0491
171	XB.PS17	37.2934	-5.3916
172	XB.PS18	37.2498	-4.7376
173	XB.PS19	37.3716	-4.9943
174	XB.PS21	37.3446	-4.4559
175	XB.PS22	37.3658	-4.7038
176	XB.PS23	37.5602	-5.1014
177	XB.PS24	37.6071	-5.4031
178	XB.PS26	37.722	-4.9634
179	XB.PS30	37.836	-4.9038
180	XB.PS33	38.1574	-4.9056
181	XB.PS34	38.4335	-4.7503
182	XB.PS35	38.7136	-4.8819
183	XB.PS37	38.9997	-4.9555

184	XB.PS39	39.3947	-5.0049
185	XB.PS40	39.4862	-4.8449
186	XB.PS41	36.667	-5.9442
187	XB.PS42	36.5282	-5.0434
188	XB.PS44	36.3173	-5.9889
189	XB.PS45	36.3055	-5.7158
190	XB.PS46	36.8236	-4.3411
191	XB.PS47	36.8698	-4.0794
192	XB.PS48	36.9012	-3.7271
193	XB.PS49	36.9033	-3.1827
194	XB.PS51	36.973	-4.8873
195	XB.PS52	37.0036	-4.2263
196	XB.PS53	37.057	-3.9636
197	XB.PS56	37.1101	-3.4368
198	XB.PS57	37.0115	-2.9864
199	XB.PS58	37.2636	-3.9969
200	XB.PS59	37.3241	-3.7995
201	XB.PS60	37.3267	-3.4519
202	XB.PS61	37.2887	-3.0686
203	XJ.LN15	-2.6279	36.1846
204	XJ.NG54	-2.7316	35.3595
205	XK.W01PD	-13.7073	33.0061
206	XV.AMPY	-24.7033	44.7436
207	XV.ANLA	-17.7062	49.4599
208	XV.ANTS	-14.8843	47.9993
209	XV.BAEL	-14.5397	48.7467
210	XV.BAND	-20.3428	45.5964
211	XV.BANJ	-13.6426	48.4537
212	XV.BARY	-17.1845	46.8571
213	XV.BATG	-18.8786	46.1871
214	XV.BERG	-15.58	47.6277
215	XV.BITY	-20.0608	47.0001
216	XV.BKTA	-24.1822	45.673
217	XV.CPSM	-25.5358	45.15
218	XV.DGOS	-12.2825	49.3606
219	XV.KIRI	-20.0676	44.6595
220	XV.LAHA	-14.9344	50.2911
221	XV.LONA	-22.8057	44.2959
222	XV.MAGY	-19.3179	48.9785
223	XV.MAHA	-23.1714	47.6899
224	XV.MAJA	-15.7323	46.4263
225	XV.MAPH	-22.25	35.08
226	XV.MARO	-20.1331	44.5515
227	XV.MKVA	-14.1368	50.0608

228	XV.MMBE	-21.7501	43.3721
229	XV.MOCU	-16.86	36.83
230	XV.MSGR	-23.83	32.18
231	XV.NAPU	-15.08	39.25
232	XV.SENA	-17.445	35.032
233	XV.SOLA	-15.8636	48.8263
234	XV.TANS	-18.9176	47.5511
235	XV.TETE	-16.13	33.57
236	XV.VATO	-19.3314	48.9824
237	XV.VINA	-18.1769	45.2247
238	XV.ZAKA	-17.8471	48.423
239	XV.ZOBE	-18.1369	47.2289
240	XW.ADEN	12.77592	44.982441
241	XW.ALJZ	18.6157	56.538898
242	XW.BSRN	18.966299	55.972198
243	XW.DEMT	17.726999	55.072899
244	XW.DHAH	19.057819	57.545311
245	XW.DRAK	19.0152	57.761002
246	XW.DUQM	19.5588	57.609001
247	XW.GASH	18.4324	56.108002
248	XW.GBRA	19.091999	56.552898
249	XW.HAS3	17.489	55.217999
250	XW.HBAB	19.443199	56.721901
251	XW.HN01	17.9613	55.921001
252	XW.KRWN	19.270201	57.208099
253	XW.MADQ	16.20682	51.39719
254	XW.MIRB	16.985901	54.6973
255	XW.MKRZ	19.257799	57.596802
256	XW.MKZA	19.3696	56.3479
257	XW.NIMR	18.541401	55.8377
258	XW.OMRN	18.444599	55.303101
259	XW.RIMA	18.8311	56.3232
260	XW.SABA	18.755699	56.639999
261	XW.SADA	19.500799	57.465
262	XW.SAHL	18.901899	57.040199
263	XW.SANA	15.39263	44.206821
264	XW.SAWQ	18.1618	56.4314
265	XW.SHA2	18.1203	55.7407
266	XW.SUYR	19.560699	57.690399
267	XW.THAT	18.0093	56.271702
268	XW.WAYM	17.9153	55.6437
269	YB.AT31	38.5727	34.5084
270	YH.CHAL	-6.6403	38.367
271	YH.IFAK	-8.1397	36.6828

272	YH.INDI	-10.0167	39.7149
273	YH.KIMA	-8.9199	39.5141
274	YH.MANG	-7.1981	38.7733
275	YH.MOHO	-8.1426	39.1832
276	YH.MTWA	-10.2776	40.194
277	YH.WALE	-9.7896	37.917
278	YI.AAIR	-9.9546	33.8955
279	YQ.MAKE	-9.2647	34.0968
280	YQ.MZUN	-9.1502	33.5213
281	ZP.CHAM	-10.9505	31.0691
282	ZP.CHIM	-8.8263	34.0284
283	ZP.GABZ	-12.171	26.367
284	ZP.IRIN	-7.762	35.6864
285	ZP.ISOK	-10.1708	32.6457
286	ZP.KAMZ	-14.7948	24.8044
287	ZP.KASM	-10.2174	31.1401
288	ZP.KGMA	-4.878	29.633
289	ZP.KISH	-12.0219	29.6123
290	ZP.KISZ	-12.1116	25.4952
291	ZP.KMPZ	-13.4568	25.8337
292	ZP.KYLA	-9.5986	33.8673
293	ZP.LAEL	-8.566	32.0591
294	ZP.LOSS	-8.4166	33.1575
295	ZP.LWNG	-10.2498	29.921
296	ZP.MAFI	-8.3057	35.3132
297	ZP.MAKA	-8.8465	34.8302
298	ZP.MANS	-11.14	28.8749
299	ZP.MAUS	-2.741	36.704
300	ZP.MGOR	-6.8279	37.6696
301	ZP.MIKU	-7.4035	36.9902
302	ZP.MKUS	-13.6035	29.3791
303	ZP.MPIK	-11.821	31.4517
304	ZP.MUFZ	-13.1442	25.0213
305	ZP.MWEN	-10.0582	28.7017
306	ZP.NAMA	-7.5094	31.0414
307	ZP.NJOM	-9.3665	34.7911
308	ZP.PNDA	-6.3519	31.0613
309	ZP.SERJ	-13.2275	30.215
310	ZP.SHWG	-11.1925	31.7397
311	ZP.SONG	-10.6738	35.6507
312	ZP.SUMB	-7.9531	31.6195
313	ZP.TUND	-9.2958	32.7712
314	ZP.UVZA	-5.1049	30.3934
315	ZP.WINO	-9.7576	35.3001

316	ZR.ABAE	13.3535	39.76355
317	ZR.AFME	13.20396	40.858479
318	ZR.AHME	14.08887	40.2784
319	ZR.ASYE	11.5607	41.4422
320	ZR.BIME	12.84183	40.98386
321	ZR.BTIE	11.1949	40.021801
322	ZR.DALE	14.22897	40.217831
323	ZR.DAME	11.68684	40.96249
324	ZR.ERTE	13.4463	40.496899
325	ZR.FINE	12.06812	40.315971
326	ZR.GALE	13.72514	40.394009
327	ZR.GPSE	13.48817	40.528332
328	ZR.GULE	13.69449	39.588539
329	ZR.HALE	13.84221	40.007721
330	ZR.HITE	13.10124	40.31691
331	ZR.IGRE	12.25259	40.461231
332	ZR.KOZE	12.49478	40.98489
333	ZR.LULE	11.98922	40.703701
334	ZR.MAYE	12.7832	39.534302
335	ZR.SAHE	12.04015	40.976952
336	ZR.SEME	11.79258	41.00433
337	ZR.TRUE	12.48125	40.314812

Appendix B

Solver Parameter file

```
# forward or adjoint simulation
SIMULATION_TYPE                 = 1
NOISE_TOMOGRAPHY                = 0
SAVE_FORWARD                    = .false.

# number of chunks (1,2,3 or 6)
NCHUNKS                         = 1

# angular width of the first chunk (not used if full sphere with six chunks)
ANGULAR_WIDTH_XI_IN_DEGREES   = 140.d0      # angular size of a chunk
ANGULAR_WIDTH_ETA_IN_DEGREES  = 140.d0
CENTER_LATITUDE_IN_DEGREES    = -9.d0
CENTER_LONGITUDE_IN_DEGREES   = 12.d0
GAMMA_ROTATION_AZIMUTH        = 0.d0

# number of elements at the surface along the two sides of the first chunk
# (must be multiple of 16 and 8 * multiple of NPROC below)
NEX_XI                          = 288
NEX_ETA                         = 288

# number of MPI processors along the two sides of the first chunk
NPROC_XI                        = 12
NPROC_ETA                       = 12

MODEL                           = CEM_ACCEPT

# parameters describing the Earth model
OCEANS                          = .true.
ELLIPTICITY                     = .true.
```

```
TOPOGRAPHY                      = .true.
GRAVITY                         = .true.
ROTATION                        = .true.
ATTENUATION                     = .true.

ABSORBING_CONDITIONS            = .true.

RECORD_LENGTH_IN_MINUTES        = 45.0d0

MEMORY_INSTALLED_PER_CORE_IN_GB = 25.d0

PERCENT_OF_MEM_TO_USE_PER_CORE  = 100.d0

EXACT_MASS_MATRIX_FOR_ROTATION  = .false.

USE_LDDRK                       = .false.

INCREASE_CFL_FOR_LDDRK          = .true.
RATIO_BY_WHICH_TO_INCREASE_IT   = 1.5d0

MOVIE_SURFACE                   = .false.
MOVIE_VOLUME                    = .false.
MOVIE_COARSE                    = .true.
NTSTEP_BETWEEN_FRAMES           = 50
HDUR_MOVIE                      = 0.d0

MOVIE_VOLUME_TYPE               = 2
MOVIE_TOP_KM                    = -100.0
MOVIE_BOTTOM_KM                 = 1000.0
MOVIE_WEST_DEG                  = -90.0
MOVIE_EAST_DEG                  = 90.0
MOVIE_NORTH_DEG                 = 90.0
MOVIE_SOUTH_DEG                 = -90.0
MOVIE_START                     = 0
MOVIE_STOP                      = 40000

SAVE_MESH_FILES                 = .true.

NUMBER_OF_RUNS                  = 1
NUMBER_OF_THIS_RUN              = 1

LOCAL_PATH                      = ./DATABASES_MPI
LOCAL_TMP_PATH                  = ./DATABASES_MPI

NTSTEP_BETWEEN_OUTPUT_INFO      = 10000

NTSTEP_BETWEEN_OUTPUT_SEISMOS   = 5000000
```

```
NTSTEP_BETWEEN_READ_ADJSRC      = 1000

OUTPUT_SEISMOS_ASCII_TEXT       = .false.
OUTPUT_SEISMOS_SAC_ALPHANUM     = .false.
OUTPUT_SEISMOS_SAC_BINARY       = .true.
OUTPUT_SEISMOS_ASDF             = .false.

ROTATE_SEISMOGRAMS_RT           = .false.

WRITE_SEISMOGRAMS_BY_MASTER     = .false.

SAVE_ALL_SEISMOS_IN_ONE_FILE    = .false.
USE_BINARY_FOR_LARGE_FILE       = .false.

RECEIVERS_CAN_BE_BURIED         = .true.

PRINT_SOURCE_TIME_FUNCTION      = .false.

#-----------------------------------------------------------
#
#  adjoint kernel outputs
#
#-----------------------------------------------------------

# use ASDF format for reading the adjoint sources
READ_ADJSRC_ASDF                = .false.
ANISOTROPIC_KL                  = .true.
SAVE_TRANSVERSE_KL_ONLY         = .true.
APPROXIMATE_HESS_KL             = .true.
USE_FULL_TISO_MANTLE            = .true.
SAVE_SOURCE_MASK                = .false.
SAVE_REGULAR_KL                 = .false.

#-----------------------------------------------------------

#-----------------------------------------------------------


NUMBER_OF_SIMULTANEOUS_RUNS     = 1
BROADCAST_SAME_MESH_AND_MODEL   = .false.
USE_FAILSAFE_MECHANISM = .false.

GPU_MODE                        = .true.
GPU_RUNTIME                     = 1
GPU_PLATFORM                    = NVIDIA
GPU_DEVICE                      = Tesla
```

```
# set to true to use the ADIOS library for I/Os
ADIOS_ENABLED                   = .true.
ADIOS_FOR_FORWARD_ARRAYS        = .false.
ADIOS_FOR_MPI_ARRAYS            = .false.
ADIOS_FOR_ARRAYS_SOLVER         = .false.
ADIOS_FOR_SOLVER_MESHFILES      = .false.
ADIOS_FOR_AVS_DX                = .false.
ADIOS_FOR_KERNELS               = .false.
ADIOS_FOR_MODELS                = .false.
ADIOS_FOR_UNDO_ATTENUATION      = .true.
```